

UiO : **Department of Chemistry**
University of Oslo

Synthesis of cathode materials by liquid injection system in vacuum

Erlend Hall
Project assignment, Spring 2018



Synthesis of cathode materials by liquid injection system in vacuum

Erlend Hall



Thesis submitted for a project assignment in Materials, Energy
and Nanotechnology
20 credits

Department of Chemistry
Faculty of mathematics and natural sciences

UNIVERSITY OF OSLO

Spring 2018

Preface

This thesis represents a part of the bachelor's degree in Materials, Energy and Nanotechnology at the University of Oslo. The work has been conducted at the Nanostructures and Functional Materials (NAFUMA) research group at the department of chemistry in the period of January 2018 to June 2018.

First and foremost I would like to thank my supervisors Professor Ola Nilsen, Kristian Breivik Kvamme and Katja Sofie Støren Sverdlilje. Thank you for your invaluable guidance, nudges in the right direction and being there to answer questions whenever they presented themselves.

A big thanks to the NAFUMA group for being including and always keen to help. A special thanks to David Wragg for introducing me to XRD, Amund Ruud for aiding the deciphering of some slightly disheartening XRD results and Kristian Blindheim Lausund for valuable inputs on SEM and EDS.

I would also like to thank Ole Bjørn Karlsen for letting me explore my samples freely with the tabletop SEM at the Oslo Science Park. Thanks to you I am well acquainted with the surface of my samples!

Thanks to the people in Ø154 for drinking excessive amounts of coffee with me and creating a nice working environment.

Finally, the warmest thanks to Karoline. Thank you for being my partner in crime, comforter when needed and the greatest motivator of them all.

*Erlend Hall
01.06.2018
University of Oslo*

Abstract

In this thesis, a novel liquid injection system in vacuum has been used to synthesise MnO_2 , LiMn_2O_4 (LMO) and $\text{LiNi}_{0.5}\text{Mn}_{1.5}\text{O}_4$ (LNMO) from nitrate precursors directly on a current collector. The synthesised oxides naturally adhere to the surfaces present during synthesis, making a binder redundant. After preliminary tests providing a better understanding of the system, as-deposited oxides have been used as cathode materials in assembled coin cells.

The synthesised oxides have been characterized using scanning electron microscopy and X-ray diffraction showing the synthesis of LMO and LNMO to be successful. The synthesis of MnO_2 was not successful, yielding Mn_2O_3 in lieu of the desired oxide. Characterization showed that the oxides were mostly composed of hollow spheres, ranging in size from 200 nm to 10 μm .

The electrochemical properties of the cathode materials have been investigated through a variety of electrochemical analyses supporting that functional cathodes indeed have been synthesised through liquid injection. However, not all the synthesised cathodes yielded functional batteries, and not all the functional batteries showed the expected behaviour.

Nonetheless, the cathodes displayed a lower resistance than their commercial counterpart and this work may help facilitating future deposition of hollow, porous, low-resistance electrode materials for batteries through a modified liquid injection system.

Contents

| | |
|---|------------|
| Preface | iii |
| Abstract | v |
| 1 Introduction | 1 |
| 1.1 History | 2 |
| 1.2 The Li-ion battery | 2 |
| 1.2.1 Cathodes | 2 |
| 1.3 Prior work | 4 |
| 1.4 Aim of study | 5 |
| 2 Theory and Methods | 7 |
| 2.1 Electrochemistry | 7 |
| 2.2 Scanning Electron Microscope | 8 |
| 2.3 X-ray diffraction | 9 |
| 2.4 Electrochemical analysis | 10 |
| 2.4.1 Electric Impedance Spectroscopy | 10 |
| 2.4.2 Cyclic voltammetry | 10 |
| 2.4.3 Galvanostatic cycling | 11 |
| 2.5 Liquid injection system in vacuum | 11 |
| 3 Experimental design | 13 |
| 3.1 Liquid injection system | 13 |
| 3.1.1 Parameter testing | 15 |
| 3.1.2 Cathode production | 15 |
| 3.2 Precursors | 16 |
| 3.2.1 Chemicals | 16 |
| 3.3 Experimental runs | 17 |
| 3.4 X-ray diffraction | 18 |
| 3.5 Scanning electron microscopy | 18 |
| 3.6 Coin-Cell Assembly | 18 |
| 3.7 Electrochemical analysis | 19 |

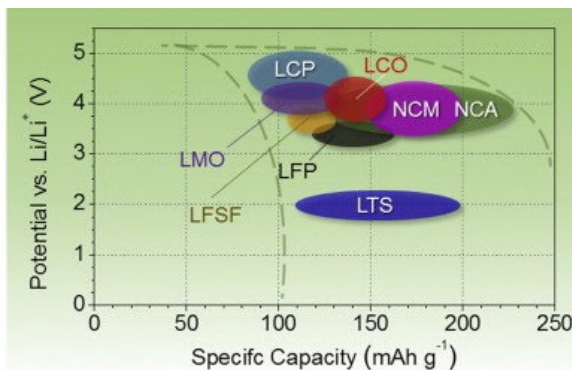
| | |
|---|-----------|
| 4 Results and Discussion | 21 |
| 4.1 Parameter testing | 21 |
| 4.2 Characterization | 23 |
| 4.2.1 SEM | 23 |
| 4.2.2 XRD | 30 |
| 4.3 Electrochemical analysis | 32 |
| 4.3.1 Electric Impedance Spectroscopy | 32 |
| 4.3.2 Cyclic Voltammetry | 33 |
| 4.3.3 Galvnostatic Cycling | 37 |
| 5 Conclusion | 39 |
| Bibliography | 41 |

Introduction

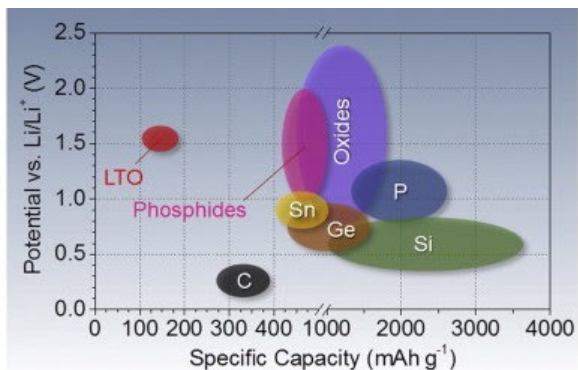
The work in this thesis consists of two parts, exploration of a new liquid injection system for the synthesis of oxides and application of this method to synthesize cathode materials directly on a current collector. These novel cathodes will not need a traditional binder in order for the cathode material to stick to the conducting surface. If this method proves to be tunable and replicable, cathodes produced by liquid injection may be able to compete with present cathodes.

Today, we surround ourselves with electricity - from electrical watches and smartphones to electrical cars and power grids. The aim for a more environmental-friendly future, together with the increasing complexity and finesse of electrical devices calls for a constant development of our technology for storing electrical energy and converting it into a usable form when required - the battery.

Batteries are commonly divided into two categories; primary and secondary batteries. Primary batteries cannot be electrically recharged and are therefore single use, whereas secondary batteries are rechargeable. The latter can offer savings in costs and resources since the batteries can be re-used instead of just disposed of when empty. A battery consists of three major parts; the anode, the electrolyte and the cathode. The cathode plays an important role when it comes to improving various aspects of batteries, such as cost, safety, power and energy densities [1]. Nowadays, the cathode is typically the most costly element, comprising about 30 % of the total price of the battery [2]. Moreover, as shown in figure 1.1, present cathode materials exhibit around half the specific capacity as the carbon anodes used today [3]. Consequently, in order to develop batteries fit for the next generation electric vehicles and energy storage systems, research into cathodes is paramount.



(a) Intercalation-type cathodes



(b) Conversion-type anodes

Figure 1.1: Approximate range of average discharge potentials and specific capacity of some of the most common electrodes in todays researched and commercial batteries [3].

1.1 History

The first electrical battery is credited to the Italian physicist Alessandro Volta who, in 1800, invented the Voltaic pile consisting of alternating disks of zinc and copper separated by brine-soaked paper [4]. Since then, a lot of different chemistries and structures have been tested. Among these we find the first rechargeable battery invented in 1859, the lead-acid battery, which to present day is being used to start internal combustion engine cars. In 1957, the typically non-rechargeable alkaline battery used in regular household devices saw the light of day. [5]

The next big breakthrough, however, came from Sony Corporation in 1991 with the pairing of a LiCoO_2 (LCO) cathode and a graphite anode to manufacture and commercialize the first mass-produced rechargeable lithium battery [6]. Li-ion batteries had been researched since 1970, starting with fundamental research into intercalation of Li into layered transition-metal sulfides and selenides [7]. Unfortunately, during recharging of these batteries, dendritic growth of Li occurred, causing the battery to short circuit by connecting the electrodes through the electrolyte solution. In 1980, John B. Goodenough and his research group found LCO to be a stable cathode material capable of donating Li-ions. Later, in 1983, Rachid Yazami was exploring Li intercalation onto graphite and found reversible Li insertion into carbon to avoid the rather pressing problem of dendrite formation [8] [5]. Akira Yoshino made use of these discoveries and invented the Li-ion battery as we know it today in 1985. This battery system comprised of a "non-aqueous secondary battery using transition-metal oxides containing lithium ion such as LiCoO_2 as a positive electrode and carbonaceous materials as a negative electrode" [8].

1.2 The Li-ion battery

The Li-ion battery (LIB) can be credited for the wireless revolution of portable computers, cell phones and tablets that has reformed global communication and is starting to reshape travel as well. As shown by companies such as Tesla, Kia and Nissan, the internal combustion engine can be replaced by a combination of a portable rechargeable battery and an electrochemical capacitor. There are, however, some imminent questions regarding cost, safety and driving range.

Li-ion batteries possess certain fundamental advantages compared to other chemistries. Li, being the third element in the periodic table, is the third lightest element and has one of the smallest ionic radii of any single charged ion. In addition, the reduction potential of Li is the lowest of any element, giving rise to the highest possible cell potential for Li based batteries. These factors allow Li-ion batteries to have an unmatchable combination of high capacity and power density [3]. However, there are some concerns. At present, Li-ion batteries are costly, and a shortage of Li and some of the currently used transition metals, such as Mn, Co and Ni, may one day become an issue [9]. Nevertheless, a significant shortage of Li is unlikely in the near future [10], [11], leaving the transition metals used in cathodes as the biggest concern at present.

1.2.1 Cathodes

A huge variety of cathodes have been researched, including, but not limited to, intercalation cathode materials, transition metal oxides, polyanion compounds and conversion cathode materials. LCO, introduced by Goodenough and commercialized by SONY, is

the first and most commercially successful type of layered transition metal oxide cathodes [3].

An intercalation cathode contains a solid host network that is able to store guest ions, which can be inserted into and removed from the host network reversibly. In a LIB, Li^+ acts as the guest ion while the host network can be metal chalcogenides, polyanion compounds or transition metal oxides. It is common to divide intercalation compounds into crystal structures, such as layered, spinel and olivine [3]. While the layered structure was the earliest form of intercalation compounds for cathodes in LIB, this thesis aims for various manganese oxides with the spinel structure.

An ideal cathode possesses high energy and power densities, is small and inexpensive. Cobalt, used in LCO, is expensive, environmentally hazardous and ethically troublesome. Amnesty warned about excessive use of child labour in cobalt mining in 2017 [12]. In comparison, manganese is a very cheap, naturally abundant and environmentally benign element, making Mn an excellent candidate for cheaper cathode materials.

The batteries assembled and tested for this thesis have consisted of various cathodes manufactured by liquid injection, aiming for MnO_2 , LiMn_2O_4 and $\text{LiNi}_{0.5}\text{Mn}_{1.5}\text{O}_4$. An anode of lithium metal and a liquid electrolyte has been used.

MnO₂

Manganese oxides are considered to be one of the most important groups of materials in energy storage science, much credited to their low cost, a high potential for nanostructuring and great diversity in the oxidation states of Mn [13]. Manganese dioxide (MnO_2) has been reported as a highly promising metal oxide for new cathode materials with a theoretical capacity of 308 mAh/g. Especially nanostructured and amorphous MnO_2 has received attention lately [14], [15].

LiMn₂O₄ (LMO)

Spinel LiMn_2O_4 has low toxicity, good safety performance and low cost and is thus considered to be an ideal cathode material for LIBs [16]. The $[\text{B}_2]\text{O}_4$ array provides a strongly bonded framework where Li^+ occupy all the tetrahedral A sites. This structure improves ion flow of the electrode, resulting in lower internal resistance and improved current handling. Unfortunately, it is difficult to extract all the lithium from LMO at practical voltages, thus limiting the capacity to around 120 mAh/g. Lithium extraction from LMO occurs at approximately 4 V.

LiNi_{0.5}Mn_{1.5}O₄ (LNMO)

By doping the spinel LMO with a certain amount of transition metal elements, for instance Ni, the Fermi energies of the material can be adjusted and their electrode potentials increased as desired [16].

Among doped spinel cathode materials, $\text{LiNi}_{0.5}\text{Mn}_{1.5}\text{O}_4$ (LNMO) has proved promising in terms of performance and discharge capacity [16]. Due to the chemical reactions taking place during cycling, LNMO shows a large charge-discharge platform at 4.7 V assigned to the redox process of $\text{Ni}^{2+}/\text{Ni}^{4+}$ and a small platform around 4 V attributed to the $\text{Mn}^{3+}/\text{Mn}^{4+}$ process.

1.3 Prior work - Synthesis of cathode materials

Cathode materials can be synthesised in many ways depending on the desired active material. A very common method is to make a slurry composed of active materials, such as LiCoO₂, conductive additives and polymeric binders. The conductive additive is used to enhance the electrode conductivity. This is achieved by filling free spaces made by the grains of active material forming a continuous network until the electrical conductivity approaches that of the conducting agent [17]. The slurry is then spread on a current collector by tape casting and can be additionally processed in order to enhance inter-particle contact and ensure good adhesion to the current collector, for instance by roll pressing.

Recently, in order to meet a demand for high-capacity electrode materials suitable for use in electric vehicles or energy storage systems, there has been research into alternative approaches for creating 'designer particles' and applying various nanostructures and composites [18]. One promising technique to achieve this is spray pyrolysis.

Spray pyrolysis

Spray pyrolysis is one of many techniques developed for the preparation of particles and films. Compared to other common processes such as chemical vapour deposition (CVD) or Sol-Gel, spray pyrolysis require simple and inexpensive equipment and is advantageous in terms of high reproducibility, easy addition of doping materials and chemical homogeneity in the final product [19]. A schematic diagram of a spray pyrolysis process is displayed in figure 1.2.

During the process, a precursor solution of aqueous or non-aqueous solvents is atomised in a droplet generating apparatus, carried by a gas into a heated reactor where it evaporates, leading to the formation of solid particles through drying, decomposition and crystallization [18], [20]. When the spray collides on a surface, the atoms spread out and interacts with other adsorbed atoms. Some of the atoms may initiate the formation of an island which can grow in size and coalesce [19].

Spray pyrolysis is to a great extent similar to the liquid injection system used in this thesis, with the distinction of the liquid injection system operating under vacuum. The introduction of vacuum causes the solvent to evaporate and the nitrates to decompose at lower temperatures. In addition to lowering the required temperature, this can lead to less sintering and decrease the particle size [18].

The adhesion of the synthesised particles to surfaces may be a direct consequence of the vacuum, and presents a distinction from conventional spray pyrolysis at the temperatures used in this thesis .

Some authors have proposed good adhesion to be a consequence of the solvent evaporating close to the substrate and the precursor being volatilised and adsorbed onto the surface, followed by decomposition. This would correspond to a heterogenous CVD reaction [21].

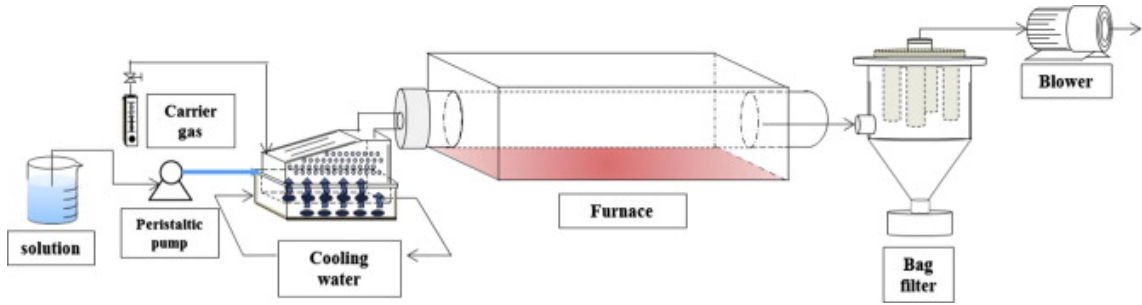


Figure 1.2: Schematic diagram of the spray pyrolysis process [18].

1.4 Aim of study

The research group has developed an injection system for the synthesis of powder. This system has proved well suited to make oxides from complex precursors. Curiously, the powder seems to adhere to the surface during synthesis. This is an effect that could prove useful to exploit for the purpose of making cathode materials for LIBs which naturally adhere to the current collector, thus not requiring any post-synthesis treatment or the addition of a polymeric binder in the synthesis.

The research performed in this thesis aims at exploring the novel method of liquid injection in vacuum and see the effects of varying different parameters. Furthermore, to utilize the system to synthesise oxides directly on conducting steel plates and assemble batteries with the as-deposited oxides as cathode materials. Electrochemical, structural and morphological studies will be performed to assess the products.

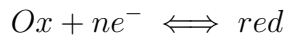
2

Theory and Methods

In the following chapter theory regarding electrochemistry, characterization and liquid injection system relevant for the project is presented.

2.1 Electrochemistry

Electrochemistry relates the flow of electrons to chemical changes, commonly seen in fuel cells and batteries. The movement of electrons from one element to another occurs through a redox reaction, relating an oxidised reactant (*Ox*) to its reduced compound (*red*), and the amount of electrons released on reduction (ne^-).



A battery consists of one or more interconnected electrochemical cells, each supplying a current (*I*) at a voltage (*V*) for a time Δt . For a battery to be rechargeable, the redox reaction occurring at the two electrodes need to be reversible.

The electrolyte separating the anode and the cathode may be liquid or solid. Liquid electrolytes are often used with solid electrodes, while a solid electrolyte commonly is in use with liquid or gaseous electrodes. With a liquid electrolyte, the electrodes are kept apart by an electrolyte-permeable separator. As can be seen from figure 2.1, the electrolyte permits the ionic component of the redox reaction (occurring at the electrodes) to pass through while forcing the electronic component to do work by traversing an external circuit.

$Q(I)$ is the cell capacity for a given current, *I*. Q is the total charge per unit weight ($\text{Ah kg}^{-1}/\text{mAh g}^{-1}$) or per volume (Ah L^{-1}). The dependency of *I* arises since the rate of transfer of ions becomes diffusion-limited at high currents.

A perfect battery would be able to dispatch the same charge on discharge as it is supplied while charging - every time. In other words, there should ideally not be any capacity fade throughout the life of the battery. A diffusion-limited loss of ions presents a reversible loss of capacity. However, changes in electrode volume, electrode decomposition or chemical reactions between electrode and electrolyte may cause an irreversible loss of capacity [22].

The Coloumbic efficiency,

$$100 \times \frac{Q_{dis}}{Q_{ch}}$$

gives the efficiency of a single cycle associated with capacity fade. The cycle life of a battery is the amount of cycles the battery can withstand before the capacity has faded to 80% of its initial reversible value.

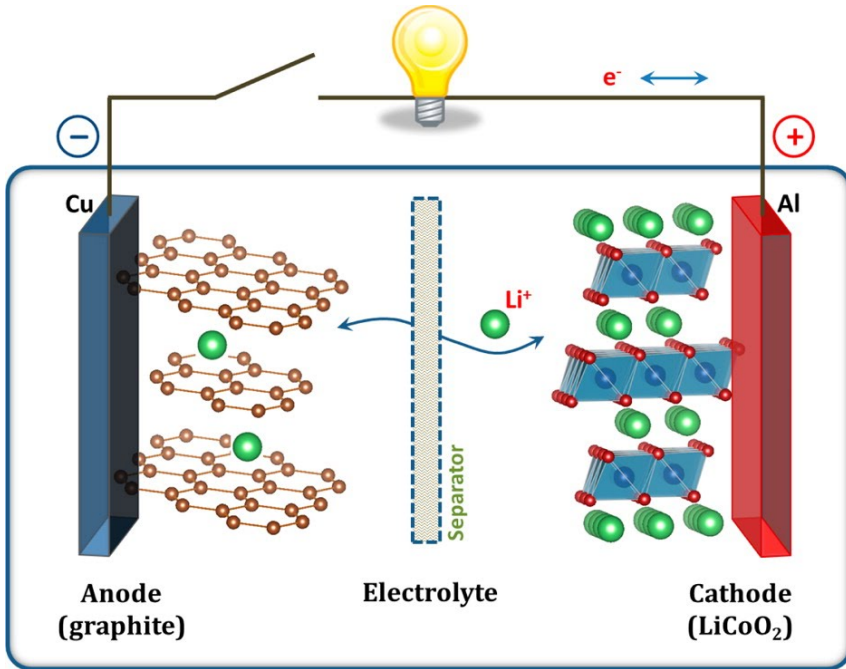


Figure 2.1: Schematic of the first Li-ion battery. Ions are permitted through the electrolyte while electrons traverse the external circuit.

Chemical reactions between electrode and electrolyte also leads to the irreversible formation of a passivating solid-electrolyte interface (SEI) on the anode. A SEI is formed during charging and compete with the reversible lithium intercalation [23]. While a SEI contributes to a capacity fade of the cell, it also enhances the stability and safety of the battery serving as a barrier between the electrode and electrolyte.

2.2 Scanning Electron Microscope

The scanning electron microscope (SEM) scans a focused electron beam over the surface area of a specimen, exploring the microscopic structure with a higher resolution and much greater depth of field compared to an optical microscope. The large depth of field results in a three-dimensional appearance of the resulting images. In addition, chemical information from a specimen can be obtained through the use of various techniques, including using a X-ray energy-dispersive spectrometer (EDS).

A SEM is composed of an electron gun and a series of electromagnetic lenses and apertures as depicted in figure 2.2. Energetic electrons striking a specimen may be scattered elastically (backscattered electrons) or inelastically (secondary electrons), or simply pass through without being scattered. Due to difference in energy and angle of the reflected and transmitted electrons, the three types can be measured by different detectors, each providing different types of image production. Figure 2.2 shows the structure of a SEM (left) and the interaction zone of electrons and atoms below a specimen surface (right) indicating the penetration depth of the various electrons.

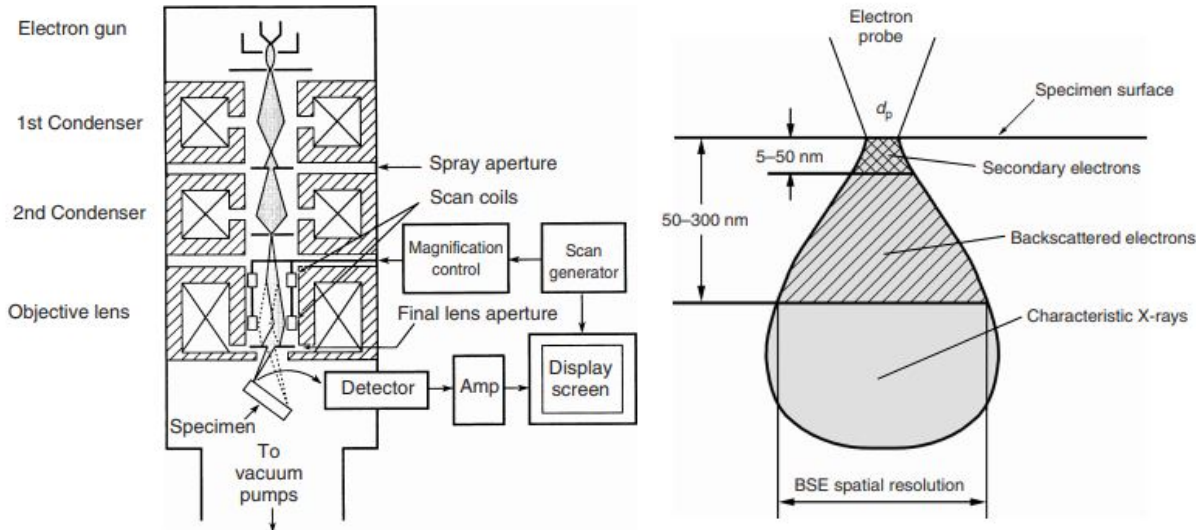


Figure 2.2: The structure of a SEM (left) [24] and the interaction zone where electrons scatter below the specimen surface (right) [25].

2.3 X-ray diffraction

X-rays are a form of electromagnetic radiation with wavelengths ranging from 0.1 to 100 Å, first discovered by Wilhelm C. Röntgen in 1895. These wavelengths are in the order of interatomic distances in crystals causing diffracted waves to form a unique diffraction pattern due to interference. Thus, X-rays have proven to be an excellent probe of the structure of matter [26], [27].

The condition for constructive interference is described by Bragg's law as

$$n\lambda = 2d \sin \theta$$

where n is an integer, d is the lattice spacing, λ is the wavelength of the diffracted beam and θ is the diffraction angle. An illustration of the geometry is shown in figure 2.3.

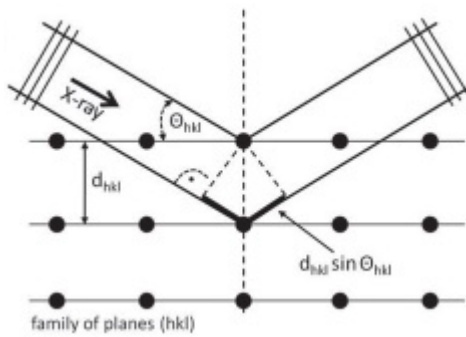


Figure 2.3: Visualization of the principles used to derive Bragg's law [27].

By plotting the counted reflections as a function of the angle between the incident and the diffracted beam (angle of diffraction), the positions and intensities of the peaks function as a fingerprint for the identification of unknown materials by comparing the diffraction pattern with a reference database. Further comprehensive analysis can supply information regarding bond lengths, bond angles, structural disorder and more [27].

2.4 Electrochemical analysis

When investigating the electrochemical properties of a battery, the cell voltage and the current are often the main parameters of interest. With one of these parameters fixed and the other monitored, valuable information regarding the electrochemical properties can be obtained. The techniques utilised in this thesis are Electric Impedance Spectroscopy (EIS), Cyclic Voltammetry (CV) and Galvanostatic Cycling (GC).

2.4.1 Electric Impedance Spectroscopy

Impedance is a measurement of the opposition a circuit presents to a current, or a change in current, with an applied voltage. Impedance possesses both magnitude and phase and extends the concept of resistance to alternating current (AC) circuits. Thus, impedance is said to be a broadened description of Ohm's law, being a complex value where the real part (Re) is the Ohmic resistance and the imaginary part (Im) represents capacitance and inductance.

To measure the electrochemical impedance a sinusoidal AC-voltage is usually applied to an electrochemical cell and the current signal is measured. By doing this for a range of frequencies one obtains a measured spectrum which can be used to analyse different charge carriers present in the battery. The results from EIS sweeps are often presented in a Nyquist plot, plotting $\text{Re}(Z)$ vs. $\pm \text{Im}(Z)$.

2.4.2 Cyclic voltammetry

CV is a highly versatile and useful technique commonly employed to investigate the reduction and oxidation properties of a given material. In addition, CV is used to study electron transfer-initiated chemical reactions [28]. During CV, current is measured as a function of applied voltage. With a minimum and maximum voltage set, the measurement starts at zero current voltage (0CV). From there, the voltage is swept at a constant scan rate to the maximum voltage, then to the minimum voltage and ends up at 0CV. This scan is repeated for a number of cycles. Figure 2.4 shows a typical CV plot containing the classical "duck" shape. Peaks corresponding to chemical reactions occurring in the battery are present at B and D and the direction of the voltage is changed at C and E.

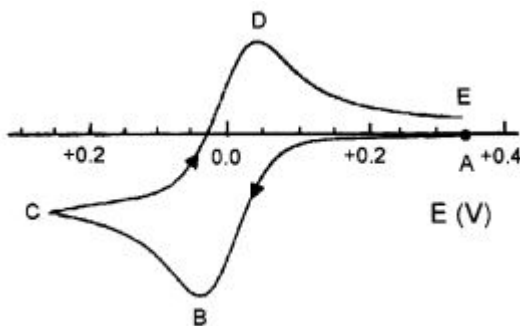


Figure 2.4: A typical cyclic voltammetric profile. The peaks at B and D correspond to chemical reactions occurring in the battery, while C and E is where the applied voltage is reversed [29].

2.4.3 Galvanostatic cycling

During GC a constant current is forced into or out of the battery. The cell is cyclically charged and discharged at a constant current between voltage limits defined by the chemistry of the battery and the voltage is recorded as a function of time. Figure 2.5 shows the different stages during a measurement. GC provides insight about the specific capacity, lifetime and cycling stability of the battery cell at different current densities [30].

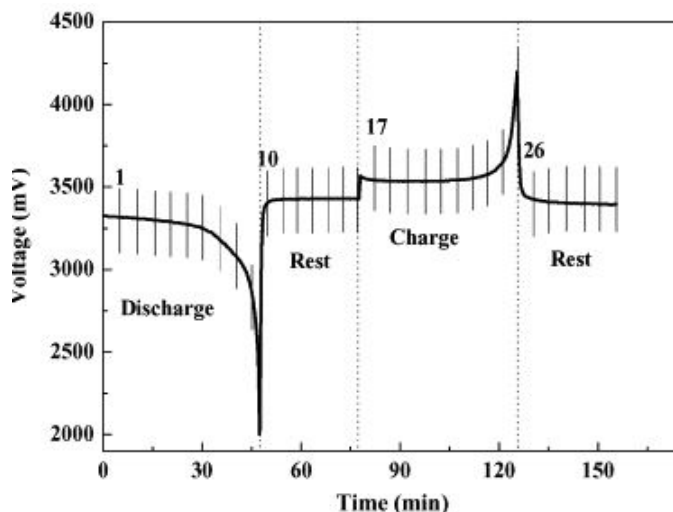


Figure 2.5: The different stages during a GC measurement [31].

2.5 Liquid injection system in vacuum

The main goal of this thesis is to explore a novel system for the formation of oxides from a variety of more or less complex compounds. The system produces powder that sticks to the surfaces present during synthesis. Liquid is injected in pre-determined amounts (droplets) into a round bottom flask under vacuum and heated. The solvent evaporates and the precursor decomposes into oxides which are then deposited on the substrates present in the flask as well as the surface of the flask itself.

As explained in the introduction, this system is similar to spray pyrolysis with the exception of this process to operate under vacuum. Due to the vacuum, the synthesised oxides adhere surprisingly well to the surfaces present and seems to disperse in the entire chamber, which in this case is a round-bottom flask.

This behaviour can be exploited to synthesize cathodes without the need for a binder in order to have the oxide stick to a conducting surface and will be covered extensively in the following section.

3

Experimental design

This section intends to give an overview of the instrumentation used in this thesis. Since the deposition technique used is a new method, the level of detail will be more extensive.

3.1 Liquid injection system

The system consisted of a 500 ml single-neck round-bottom flask with a joint size of 29/32 (29 mm wide at the top and 32 mm long) attached to a connector pipe, sealed with a Teflon cone and silicon grease. A 1/16" stainless steel tube, henceforth called injector tube, went from a 6-port Valco valve through a cap on top of the connector tube, and down to the bottom of the neck of the flask. A vacuum pump was connected to the connector tube in order to reduce the pressure of the flask, and the pressure was monitored with the use of a Pirani gauge. A heating mantle and aluminium foil was used to heat the round-bottom flask to 300-400 °C during the injection.

In addition to the injector tube, the 6-ports valve connects a 10 mL syringe containing the precursor, a steel tube forming a loop, an open-end tube and a tube supplying nitrogen gas. The 6-ports valve was used in two different positions, controlled by an Arduino. The first position allowed for the tube to be filled with the precursor. The precursor was mechanically injected from the syringe, and any excess liquid went into a waste beaker from the open-end tube. The second position enabled a nitrogen flow to push the liquid from the tube through the injector tube and into the round-bottom flask. A schematic of the apparatus is presented in figure 3.1 where the two positions termed a) and b) are shown with dashed lines representing the active channels for each position.

Two different vacuum pumps were used due to malfunction of the first pump halfway through the experiments. The first was a rotary vane pump and the second a membrane pump.

During the preparation for new runs a round-bottom flask was washed and dried, 10 mL of the precursor solution measured in the syringe, and all the substrates blown and washed with ethanol before carefully placing them in the flask. A variety of glass, Si and steel plates were utilised. Between the runs, the round-bottom flasks were washed in an acid bath, removing most of the deposited material from the previous run. Any residual material that did not get washed away with either acid or water and a brush were thought not to affect the consecutive run.

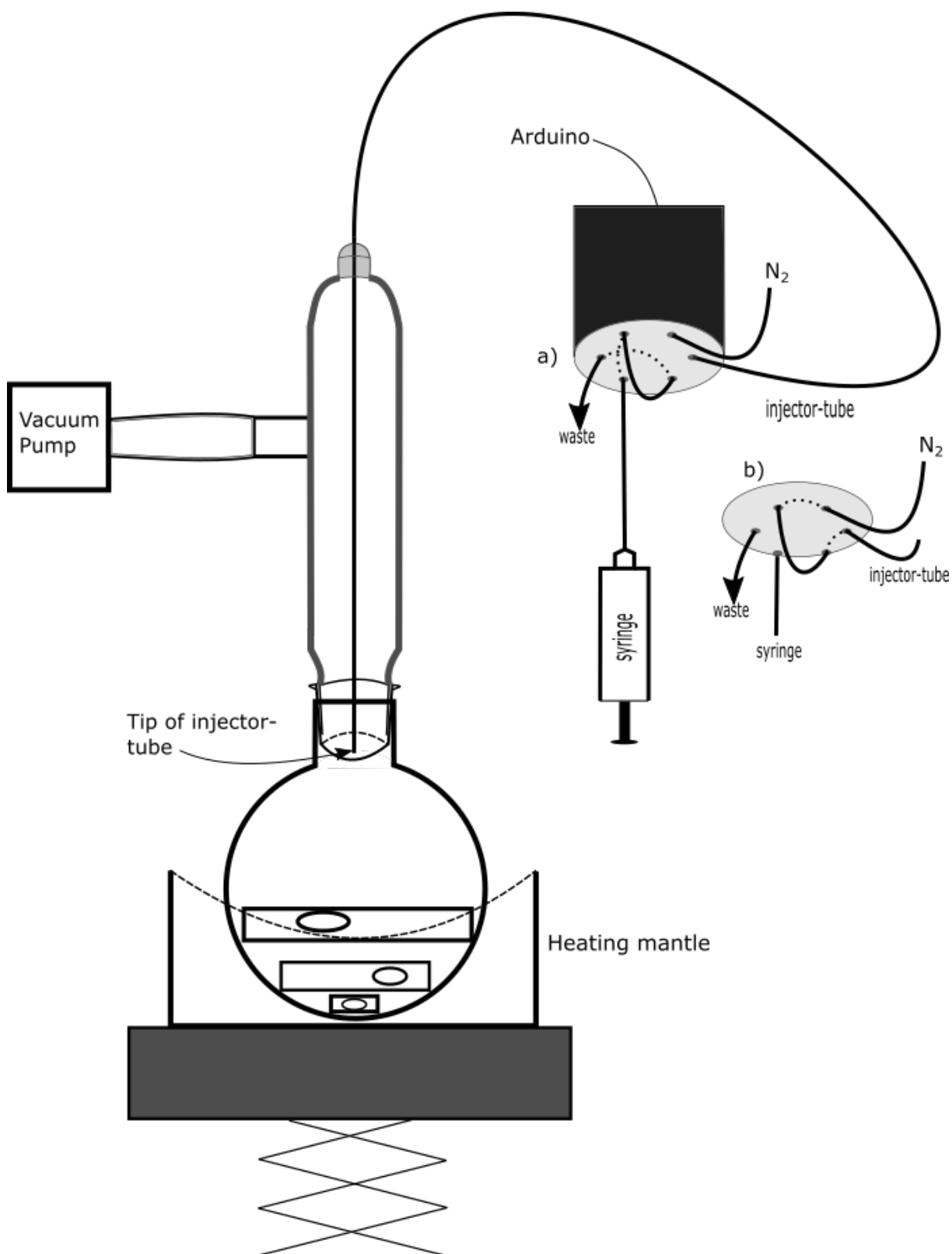


Figure 3.1: Schematic of the liquid injection system. The different channels active for the two positions are marked a) and b).

3.1.1 Parameter testing

Since this is a novel system, various parameters have been altered in order to see their effect on the synthesised material. The main parameters of interest have been the position of the tip of the injector-tube, affecting the distance the droplets travel before reaching the surface, and the concentration of the precursor(s). Additionally, the placement of the substrates has been investigated. Figure 3.2 shows the tip of the injector tube (left) and a holder fabricated for one steel substrate (right). The holder was utilised, but using a little ethanol to make a steel substrate stick to a glass substrate was found to work just as well.

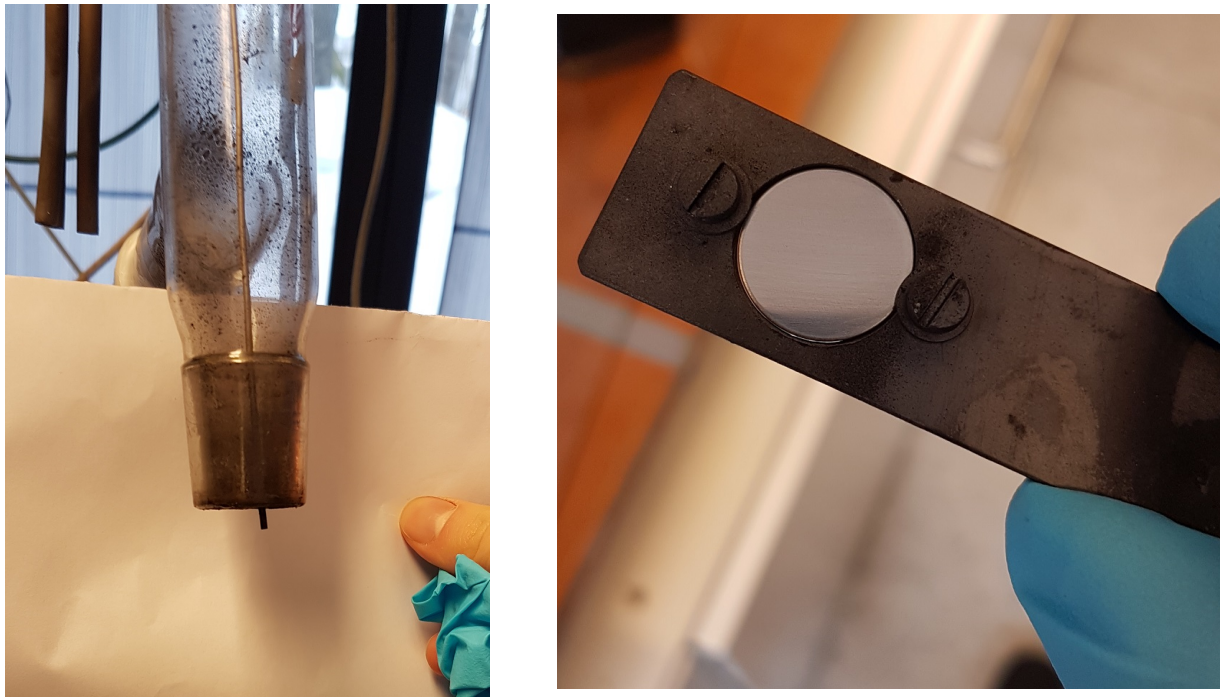


Figure 3.2: Images of the tip of the injector tube (left) and the holder fabricated to hold one steel substrate (right).

3.1.2 Cathode production

When the parameters proved satisfactory with respect to the synthesised oxides appearing replicable and providing a good particle distribution through SEM inspection, the parameters were kept constant and two sets of cathode materials were synthesised for the assembly of coin cells, 0.25 M and 2.50 M of cations in the precursor solution, trying to synthesise MnO_2 , LMO and LNMO. This is further explained in section 2.3. Very important during these sets of syntheses was the ability to keep parameters consistent. Straight after synthesis, the system was allowed to cool down while still having an inert atmosphere due to the vacuum. As soon as the vacuum was broken, the steel substrates were weighed and moved to a glove box awaiting coin cell assembly.

The setup used, later termed setup A, is shown in figure 3.3. The setup referred to as setup B is similar, except for the bottom steel substrate placed beneath the topmost glass, just lying on the substrate holder. This did not have any visible effect and setup A was resumed.



Figure 3.3: Image of setup A.

3.2 Precursors

Metal nitrates (hydrates) are popular precursor components for the preparation of oxides, and their decomposition is well documented [32]–[34].

3.2.1 Chemicals

All chemicals were used without any further purification and stored as advised by manufacturer. Table 3.1 shows the chemicals with specifications.

Table 3.1: The compounds used as precursors.

| Compound | Linear formula | Purity | Supplier | CAS | Lot # |
|--------------------------------|---|---------|---------------|------------|-----------|
| Manganese(II) nitrate hydrate | $\text{Mn}(\text{NO}_3)_2 \cdot 5 \text{H}_2\text{O}$ | 98% | Sigma-Aldrich | 15710-66-4 | MKBR0853V |
| Manganese(II) nitrate hydrate* | $\text{Mn}(\text{NO}_3)_2 \cdot 4 \text{H}_2\text{O}$ | Unknown | Unknown | Unknown | Unknown |
| Lithium nitrate | LiNO_3 | > 99% | Sigma-Aldrich | 7790-69-4 | BCBG3251V |
| Nickel(II) nitrate hydrate | $\text{Ni}(\text{NO}_3)_2 \cdot 6 \text{H}_2\text{O}$ | Unknown | KEBO | 9650672 | 6721 |

*Due to shortage of the Manganese(II) nitrate hydrate from Sigma-Aldrich, an old batch found in a closet was used for the last set of runs.

Stoichiometry

In order to verify the stoichiometry of the synthesised oxides, 1mL of the prepared solution was measured into a weighed glass vial, left in a oven at 60 °C until most of the solvent had evaporated, and then placed in a furnace holding 400 °C for a couple minutes until the nitrates had decomposed into oxides. A new weighing of the glass vial supplied the mass of the synthesised oxide, making it possible to calculate the stoichiometry required for the number of moles of the precursor(s) to match the number of moles of the synthesised oxide. This approach was also used to verify the degree of hydration for the two $\text{Mn}(\text{NO}_3)_2 \cdot x\text{H}_2\text{O}$ used.

3.3 Experimental runs

The water used as solvent was ASTM type II water. The concentration of cations in the precursors will be used to distinguish the different oxides.

MnO₂

For the first set of testing, 12 mmol of $\text{Mn}(\text{NO}_3)_2 \cdot 5\text{H}_2\text{O}$ was dissolved in water and diluted to a concentration of 0.120 M. The solution was mixed well and used in the synthesis as explained in section 3.1.

To make a solution of increased concentration, 12.6 mmol of $\text{Mn}(\text{NO}_3)_2 \cdot 5\text{H}_2\text{O}$ was dissolved in 50 mL water, yielding a concentration of 0.252 M.

For the further ten-fold increase in concentration, the Manganese(II) nitrate hydrate marked with an asterix in table 3.1 was used. 62.52 mmol of $\text{Mn}(\text{NO}_3)_2 \cdot 4\text{H}_2\text{O}$ was dissolved in 25 mL water, yielding a concentration of 2.50 M.

LMO

In order to synthesise LMO, LiNO_3 and $\text{Mn}(\text{NO}_3)_2 \cdot 5\text{H}_2\text{O}$ were weighed out to obtain the molar ratio of metal components (Li:Mn) of 1:2 and dissolved to prepare aqueous solutions of 0.252 and 2.5 M. (4.2 [20.83] mmol LiNO_3 and 8.39 [41.67] mmol $\text{Mn}(\text{NO}_3)_2 \cdot 5\text{H}_2\text{O}$ were dissolved separately and mixed to a solution of 50 [25] mL).

LNMO

To synthesise LNMO, LiNO_3 , $\text{Ni}(\text{NO}_3)_2 \cdot 6\text{H}_2\text{O}$ and $\text{Mn}(\text{NO}_3)_2 \cdot 5\text{H}_2\text{O}$ were weighed out to obtain the molar ratio of metal components (Li:Ni:Mn) of 1:0.5:1.5 and dissolved to prepare aqueous solutions of 0.252 and 2.5M. (4.20 [20.85] mmol LiNO_3 , 2.10 [10.41] mmol $\text{Ni}(\text{NO}_3)_2 \cdot 6\text{H}_2\text{O}$ and 6.31 [31.24] mmol $\text{Mn}(\text{NO}_3)_2 \cdot 5\text{H}_2\text{O}$ were dissolved separately and mixed to a solution of 50 [25] mL).

Table 3.2: Table of the different runs conducted.

| Experiment | Concentration of cations | Precursor(s) | Substrates | Notice |
|--------------------|--------------------------|--------------|---------------------------|--|
| Testing parameters | | | | |
| 01 | 0.120 M | Mn | 1x Glass, 1x Si | First run |
| 02 | 0.120 M | Mn | 1x Glass, 1x Si | Duplicate of experiment 01 |
| 03 | 0.120 M | Mn | 1x Glass, 1x Si | Injector wire 1 cm up from run 001 |
| 04 | 0.120 M | Mn | 1x Glass, 1x Si | Injector wire 1 cm down from run 001 |
| 05 | 0.120 M | Mn | 1x Glass | Injector wire 2 cm down from run 001 |
| 06 | 0.120 M | Mn | 1x Glass, 1x Steel | Steel plate positioned below glass |
| 07 | 0.120 M | Mn | 1x Glass, 1x Steel | Steel plate positioned above glass |
| 08 | 0.120 M | Mn | 1x Steel | Sample holder hung vertically from the wire |
| 09 | 0.120 M | Mn | 1x Glass, 1x Steel | Sample holder adjusted |
| 10 | 0.252 M | Mn | 1x Glass, 1x Steel | Sample holder placed horizontally. Injector wire changed |
| 11 | 0.252 M | Mn | 1x Glass, 1x Steel | Duplicate of experiment 10 |
| 12 | 0.252 M | Mn | 1x Glass, 1x Steel | Duplicate of experiment 10 |
| Setup fixed | | | | |
| 13 | 0.252 M | Li, Mn | 2x Glass, 3x Steel | Setup A |
| 14 | 0.252 M | Li, Mn | 2x Glass, 2x Steel | Setup A |
| 15 | 0.252 M | Li, Mn | 3x Glass, 3x Steel | Setup B |
| 16 | 0.252 M | Li, Mn | 3x Glass, 1x Si, 2x Steel | Setup A |
| 17 | 0.252 M | Li, Mn | 3x Glass, 1x Si, 2x Steel | Setup A |
| 18 | 0.252 M | Li, Ni, Mn | 3x Glass, 1x Si, 2x Steel | Setup A |
| 19 | 0.252 M | Li, Ni, Mn | 3x Glass, 1x Si, 2x Steel | Setup A |
| 20 | 0.252 M | Li, Mn | 3x Glass, 3x Steel | Setup A |
| 21 | 0.252 M | Li, Mn | 3x Glass, 3x Steel | Setup A |
| 22 | 2.50 M | Li, Mn | 3x Glass, 3x Steel | Setup A |
| 23 | 2.50 M | Mn | 3x Glass, 3x Steel | Setup A |
| 24 | 2.50 M | Li, Ni, Mn | 3x Glass, 3x Steel | Setup A. Discarded |
| 25 | 2.50 M | Li, Ni, Mn | 3x Glass, 3x Steel | Setup A |

3.4 X-ray diffraction

X-ray diffraction was performed with a Bruker AXS D8 discover diffractometer in reflection mode. The XRD data was analysed with DIFFRAC.EVA from Bruker.

3.5 Scanning electron microscopy

Scanning electron microscopy was performed on a tabletop Hitachi TM3000 operating at 5kV, equipped with a Silicon drift EDS detector and a thermionic emission cannon using a tungsten filament.

3.6 Coin-Cell Assembly

To investigate the electrochemical properties of the synthesised cathodes, CR2032 coin cells were built using metallic lithium as the anode and the as-deposited steel plates as cathodes. The cells were assembled inside an MBraun Labmaster glovebox with argon atmosphere, and water and oxygen levels below 0.1ppm. A Whatman glass microfiber

sheet was used as the separator membrane and the liquid electrolyte consisted of 1M LiClO₄ in a 1:1 mixture of ethyl carbonate (EC) and dimethyl carbonate (DMC).

3.7 Electrochemical analysis

Cycling voltammetry and Galvanostatic cycling was performed on a MPG2 probostat from BioLogic using EC-Lab software. Impedance spectroscopy was performed on a VSP potentiostat from BioLogic, also using EC-lab software. The data from all measurements was treated in Origin and the results are presented in the following section.

4

Results and Discussion

In this chapter, findings from the preliminary tests of the liquid injection system are presented and discussed. Secondly, the characterization of the as-deposited oxides are presented. The morphology is explored with SEM and the structure is characterized by XRD. Lastly, the electrochemical results, composed of EIS, CV and GC are presented at the end.

4.1 Parameter testing

Several parameters were tuned in order to help understand the processes occurring during the injection. The position of the injector tube, the concentration of cations in the precursors and the placement of substrates were of particular interest.

Position of injector tube

The position of the injector tube is directly related to the distance between the emerging droplet and the substrate surface, as seen in section 3.1. This is shown to have a considerable effect in spray pyrolysis, affecting which processes occur mid-air, near the substrate surface and on the substrate surface. However, the different positions of the injector-tube with respect to the substrates showed no visible effect on the deposited oxides. It is worth noting that no tests were performed with the position changed in an excessive manner, the distance was never smaller than 10 cm or greater than 15 cm to the closest substrate. It is considered likely that a much lower position than what was tested will result in clogging of the injector tube due to oxides forming immediately as the drop emerges and sticks to the tube.

Substrates

Several variations in placement and covering of the substrates with respect to the injector wire were tested. Substrates placed directly in the spray zone were found to have concentrated formation of particles visible to the naked eye, probably resulting from big droplets hitting the substrate before dispersing. Substrates, especially round steel plates, placed in the bottom of the flask experienced an agglomeration of 'islands'. This lead to a realisation that for the deposited material to be as uniformly distributed as possible, the substrates should be placed in such a manner that it is not directly in the spray zone, and not at the very bottom of the flask.

Concentration of precursors

Figure 4.1 shows the round-bottom flask after synthesising MnO_2 with different concentrations of the precursor. Evidently, there was a clear increase in deposited material with an increased concentration of precursors. The particles seem to have been distributed quite evenly around the surface, making it possible to synthesise oxides on several substrates simultaneously provided that the substrates do not directly overlap. Consequently, as outlined in the experimental section, the final setup included three steel substrates distributed in the round-bottom flask. Here, a glass substrate is shielding the steel substrates from any direct spray.



Figure 4.1: The round-bottom flask after a run with low concentration (a) and high concentration (b) of precursors. Both are after synthesising MnO_2 .

With the setup fixed and the production of cathodes as the main incentive, the steel substrates were weighed before and after deposition in order to find the amount of deposited material. The recorded masses are summarised in table 4.1. Only the substrates that were used in coin cells and thus discussed further are included. Evidently, the mass of the deposited oxides increased drastically with a ten-fold concentration, with the exception of cathode 53 from the 2.50 M LNMO. Unfortunately, the first measurements present a large uncertainty since the measurements were performed on a scale with insufficient precision. This was corrected when measuring cathodes 21 and upwards with the use of a higher-precision scale.

Nevertheless, the increase in deposited material is clear, and shows that a ten-fold increase in the concentration of precursor cations increase the deposited material by a factor between 4.5 and 20 (cathode 53 treated as an outlier). However, especially for the 2.50 M precursors, there are huge variations in the deposited material for the various steel substrates. In the following discussion, due to uncertainty, only cathodes 31-33, 41,42 and 51-53 are addressed.

The cathodes numbered X1 were placed in the holder, closest to the injector tube, cathodes X2 were placed in the middle and X3 furthest away from the tube. For the runs synthesizing MnO_2 and LMO, the mass seems to be directly related to either the distance from the injector tube, the amount of other substrates shielding from the emerging droplets or a combination of these. This is not the case with LNMO. Here, the substrate in the middle has a lot of deposited material and the bottom substrate has barely got more than its low-concentration counterpart. Therefore, no conclusion can be drawn as to which placement is optimal or whether the bottom placement should be avoided.

Table 4.1: The recorded masses of the as-deposited oxides. There is an increase in the weight going from LMO to LNMO at low concentration and a further clear increase going to higher concentration.

| Oxide | 0.25 M MnO_2 | | | 0.25 M LMO | | | 0.25 M LNMO | | | 2.50 M LMO | | | 2.50 M MnO_2 | | | 2.50 M LMNO | | |
|------------------|-----------------------|------|------|------------|-------|-------|-------------|-----|-----|------------|-------|-------|-----------------------|-------|-------|-------------|-------|--|
| Cathode | 02 | 04 | 08 | 11 | 12 | 14 | 21 | 23 | 24 | 31 | 32 | 33 | 41 | 42 | 51 | 52 | 53 | |
| Mass [mg] | 0.08 | 0.07 | 0.18 | 0.075 | 0.078 | 0.072 | 0.7 | 0.7 | 0.7 | 3.307 | 2.074 | 1.717 | 2.11 | 1.633 | 3.170 | 7.927 | 0.769 | |
| Uncertainty [mg] | ± 0.15 | | | | | | ± 0.002 | | | | | | | | | | | |

4.2 Characterization - Structure and morphology

In the following section the results from the structural, compositional and morphological characterization of the synthesised oxides are presented.

4.2.1 SEM

The morphology and composition was studied using a SEM. Average particle size, distribution and shape of the particles as well as the composition were of interest. In order to make a good electrode material, an even distribution and relatively small particles are preferential [18]. There are also several authors suggesting the advantage of porous and hollow structures [15], [18].

MnO_2

In figure 4.2, SEM images of the synthesised MnO_2 at 0.25 M and 2.5M of cations are presented. In (a) and (b), the substrate (steel) is specked with particles ranging from 1 to 40 μm . The steel substrate is evident in the light-gray areas where lines after polishing can be seen. In (c) and (d), the story is quite different. The substrate is now fully covered by the synthesised particles. Moreover, the surface appears to be porous with some spherical particles distributed evenly around the surface. Comparing the figures clearly show that changing from low to high concentration increases the coverage on the substrate. It appears that a lot more material is deposited which correlates well with the behaviour seen in figure 4.1 and is the expected trend from an increase in precursor concentration.

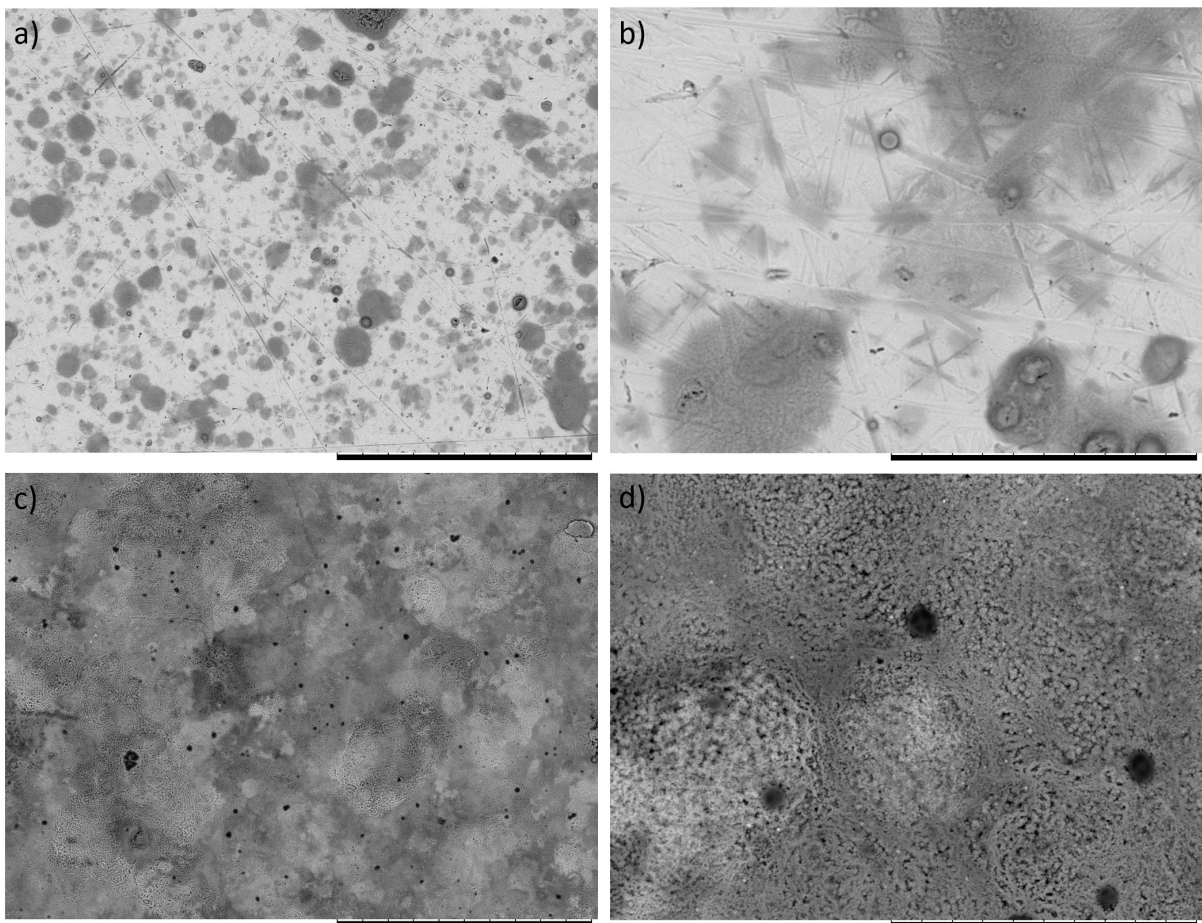


Figure 4.2: SEM images of the synthesised MnO_2 with different concentrations of cations and magnification: a,b) 0.252 M and c,d) 2.5 M. The scale bar is 300 μm for a) and c) and 50 μm for b) and d). As can be seen by comparing a,b) and c,d), the coverage has increased significantly with the increased concentration of precursors. Images a) and b) are from a steel substrate, hence the underlying lines stemming from polishing. Images c) and d) are from glass.

$LiMn_2O_4$

SEM images of the synthesised $LiMn_2O_4$ are presented in figure 4.3. Similarly to MnO_2 , the images of the lower concentration of cations (a,b) show less coverage of oxides on the surface than the high concentration (c,d) since the substrate can be clearly seen underneath, again as light-grey areas with lines from polishing apparent. There also appears to be more particles with a size around 0.5-1 μm .

The cluster of particles on the lower left-hand side of 4.3.c is shown by EDS analysis to contain an increased composition of Mn with the ratio of 1:1.1 (Mn:O) as opposed to 1:1.65 (Mn:O) on average over the rest of the sample.

The surface of (c) and (d) appears less porous than MnO_2 , but still with some porous clusters where the particles seem to have agglomerated.

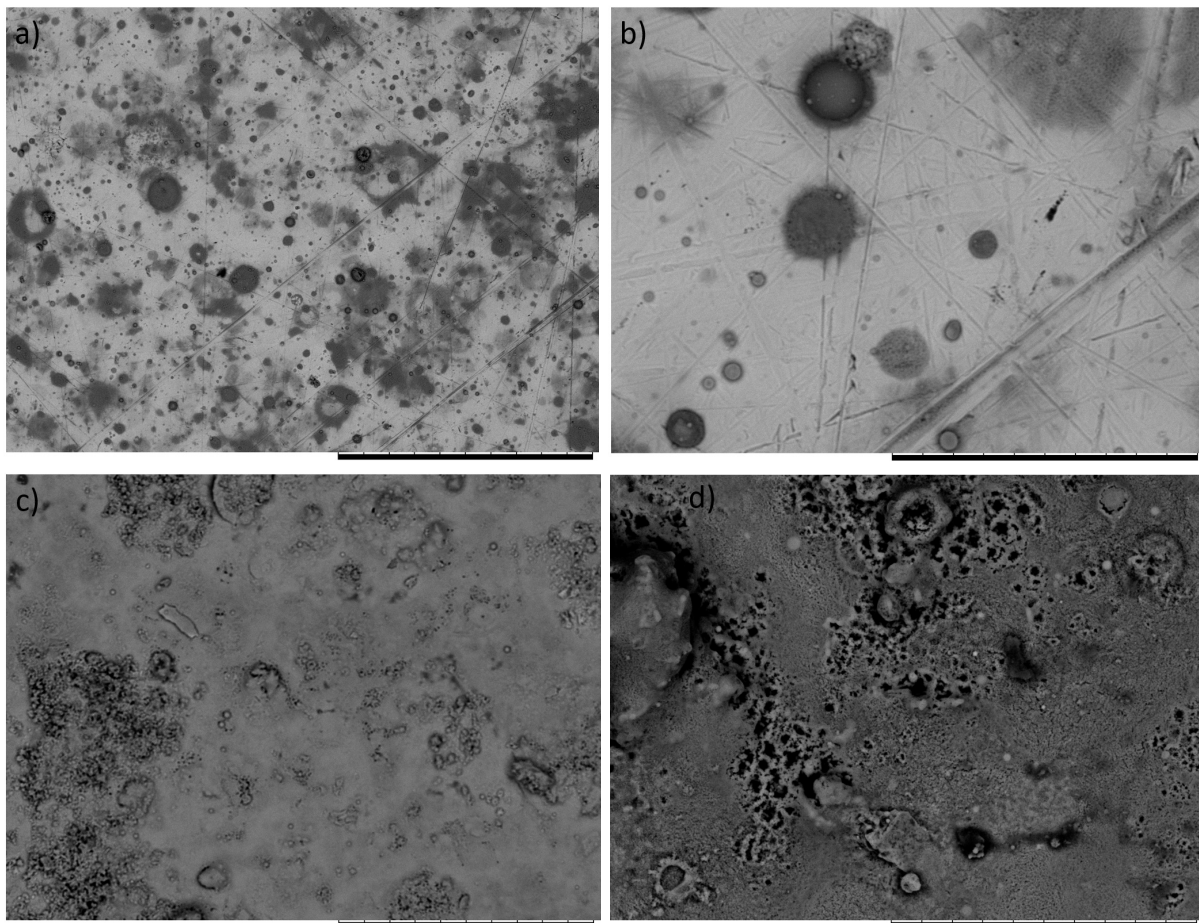


Figure 4.3: SEM images of the synthesised LiMn_2O_4 with different concentrations of cations and magnification: a,b) 0.252 M and c,d) 2.5 M. The scale bar is 300 μm for a) and c) and 50 μm for b) and c) As can be seen by comparing a,b) and c,d), the coverage has increased significantly with the increased concentration of precursors. Images a) and b) are from a steel substrate, hence the underlying lines stemming from polishing. Images c) and d) are from glass.

$\text{LiNi}_{0.5}\text{Mn}_{1.5}\text{O}_4$

Figure 4.4 shows SEM images of the synthesised $\text{LiNi}_{0.5}\text{Mn}_{1.5}\text{O}_4$. Contrary to the low-concentration images seen above, whether or not the substrate is covered by more oxides after an increased concentration is not easily deducted by a visual inspection alone. However, the EDS analysis presented in figure 4.5 shows less Na for the increased concentration (b) than the lower concentration (a). This is evident in both the composition images and the elemental analysis. In a) 10.05 at.% Na is present compared to 6.14% in b). This is due to more oxides covering the glass substrate, causing less electrons to reach the Na present in the glass substrate. Thus, the coverage has indeed increased going from 0.25 M to 2.5 M of cations in the precursor.

The low-concentration images (a and b) show a quite different morphology than what has been seen for MnO_2 and LMO. There appears to be an ensemble of crystallites with spheres of various size on top and between the grain boundaries. The crystallites are in the range of 200 nm to 1 μm . Looking closely at (b), it may look as though spheres of 5-10 μm are covered in crystallites and further have more spheres of 1-10 μm on the surface. Emerging with this theory is the notion of the surface seen in (c) and (d) being built in much the same fashion. The difference here being more and possibly even smaller

particles creating a film with some craters at the darker spot. This last claim is backed up by the elemental analysis where the Na can be seen in the spots corresponding to the dark areas, thus being more available at these spots.

Also worth noting from the EDS analysis is the even dispersion of Ni. This is highly promising since $\text{LiNi}_{0.5}\text{Mn}_{1.5}\text{O}_4$ is the desired compound.

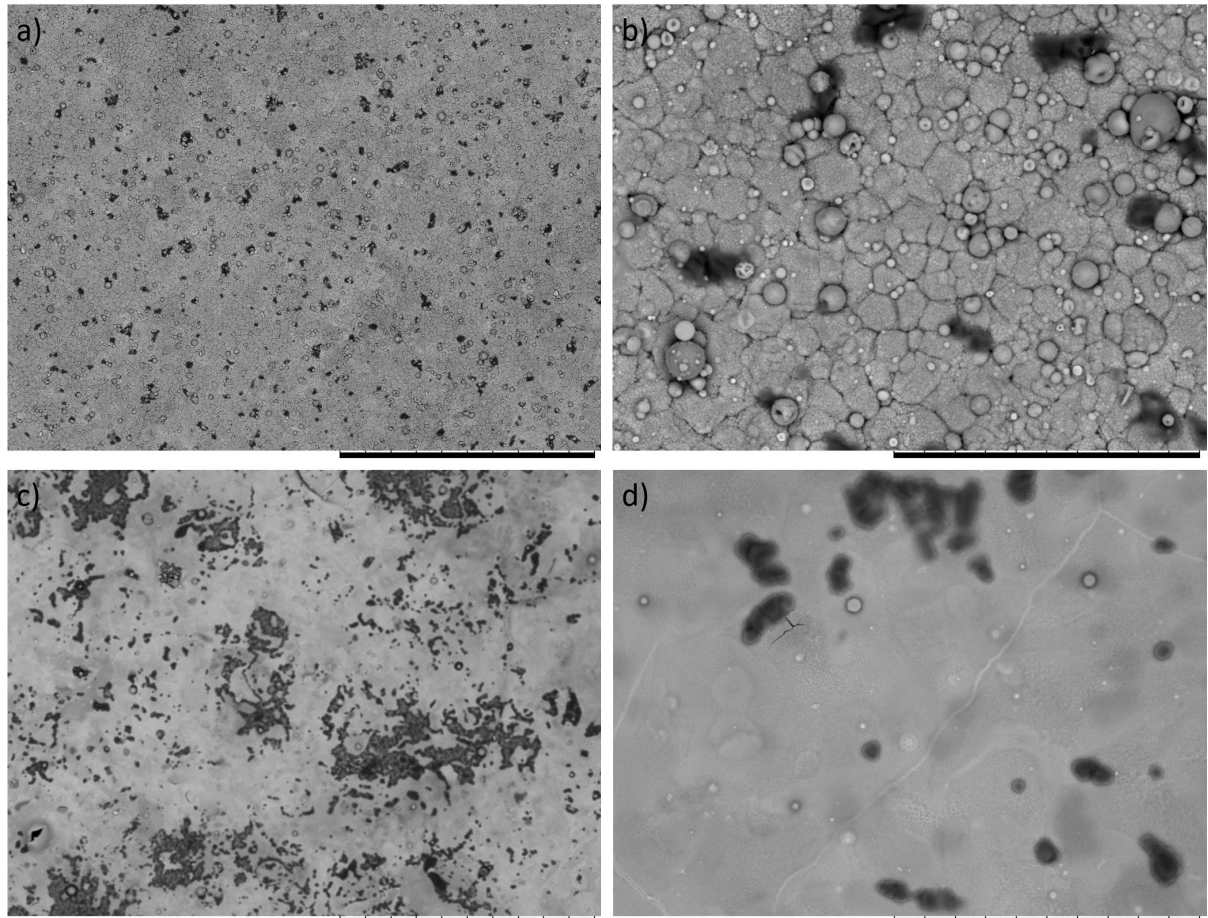


Figure 4.4: SEM images of the synthesised $\text{LiNi}_{0.5}\text{Mn}_{1.5}\text{O}_4$ with different concentrations of cations and magnification: a,b) 0.252 M and c,d) 2.5 M. The scale bar is 300 μm for a) and c) and 50 μm for b) and d) As can be seen by comparing a,b) and c,d), the coverage has increased significantly with the increased concentration of precursors. Both images are from glass substrates.

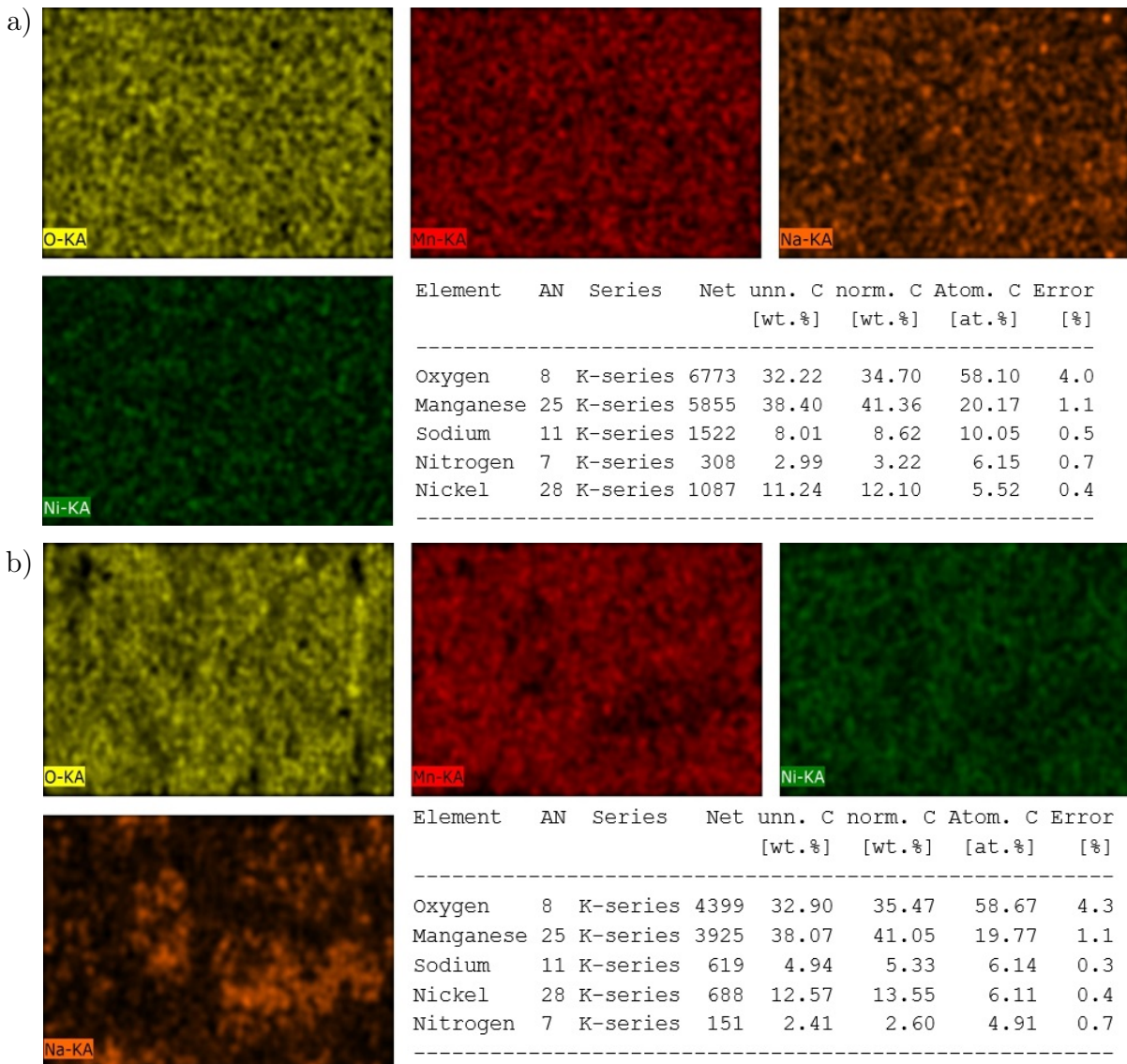


Figure 4.5: EDS images and analysis of the synthesised $\text{LiNi}_{0.5}\text{Mn}_{1.5}\text{O}_4$ with different concentrations of cations, corresponding to 0.252 M (a) and 2.5 M (b). The analysis tells us that there is an even distribution of O, Mn and Ni. Furthermore, in (b), there is less to be seen of the Na from the glass substrate indicating more deposited oxides.

Hollow spheres

Common for all the samples is an assembly of particles with different shapes. Among these, the formation of spheres is particularly interesting due to its promising structural stability and rate capability [18]. Figure 4.6 shows snippets of all the low-concentration oxides. In (a) and (b), there is evidence to suggest that the spheres are hollow with a porous inside. This is a consequence of sphere-shaped droplets having the time to dry and decompose before they hit the surface. When heated, the solvent will evaporate leaving voids in the droplet. Then an outer shell will be formed from the decomposed oxides while gas trapped inside the sphere will gather to the central cavity and expand. Looking closely at (c), the sphere here backs up the theory of droplets being covered in crystallites. Here, a sphere of 10 μm is partially covered in particles around 1 μm . Furthermore, there is another shape connected to it. This looks more like particles which have hit the surface first, then formed an island by coalescing with other adsorbed particles.

A note on droplet-particle size

Unfortunately, this technique does not offer an easy way to witness the process from droplet exiting the injector-tube, followed by the solvent evaporating and nitrate decomposing to particles striking the surface and adhering. From the SEM images, however, it looks as though the droplets entering the chamber (round-bottom flask) are varying quite a lot in size and that large droplets result in large (5-10 μm) hollow spheres and small droplets result in small (around 1 μm) hollow spheres. However, there must be some particles that do not form spheres, but rather comes crashing down on the surface to form the observed islands. These might originate from even larger droplets than the ones forming large spheres, or some intermediate-sized droplet in the range between droplets forming spheres and droplets forming crystallites.

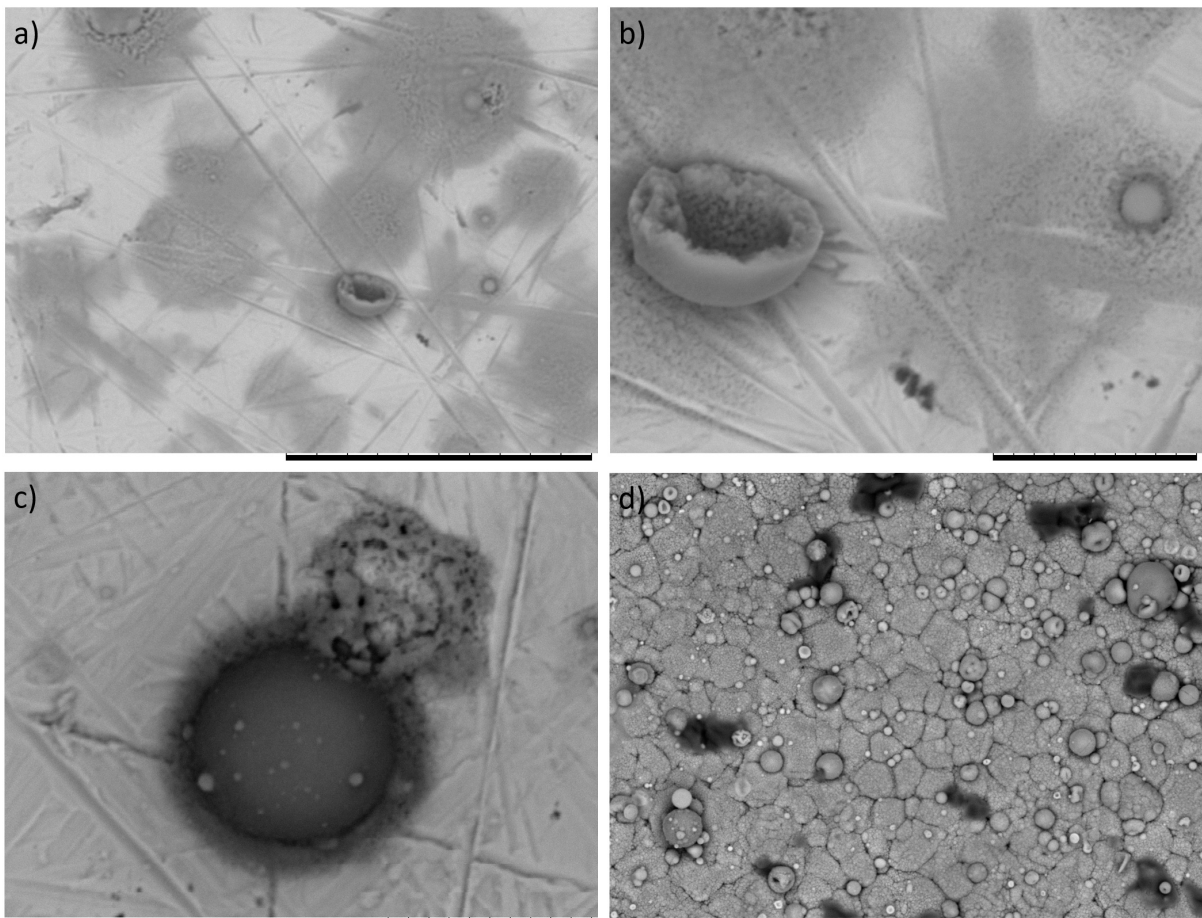


Figure 4.6: SEM images showing spherical-shaped particles for the low-concentration oxides MnO_2 (a,b), LMO (c) and LNMO (d). Images a-c) are from steel substrates. Image d) is from a glass substrate. The hollow spheres are formed as a result of droplets decomposing and drying close to the surface. The scale bar is 50 μm for a) and d) and 10 μm for b) and c).

Agglomerates

Figure 4.7 shows one of the mentioned islands from a sample of 2.50 M LNMO. These may result from an ensemble of particles interacting on the surface and agglomerating. Another possibility is that these crystals were formed before reaching the substrate, for instance by sticking to the tip of the injector-tube and growing in size until it detaches and falls down to the substrate. Based on the compositional analysis, the at.% matches that of $\text{LiNi}_{0.5}\text{Mn}_{1.5}\text{O}_4$ with some excess Mn and O. This leads to a belief that the agglomerate is mainly composed of LNMO and some crystallised derivative of manganese oxide.

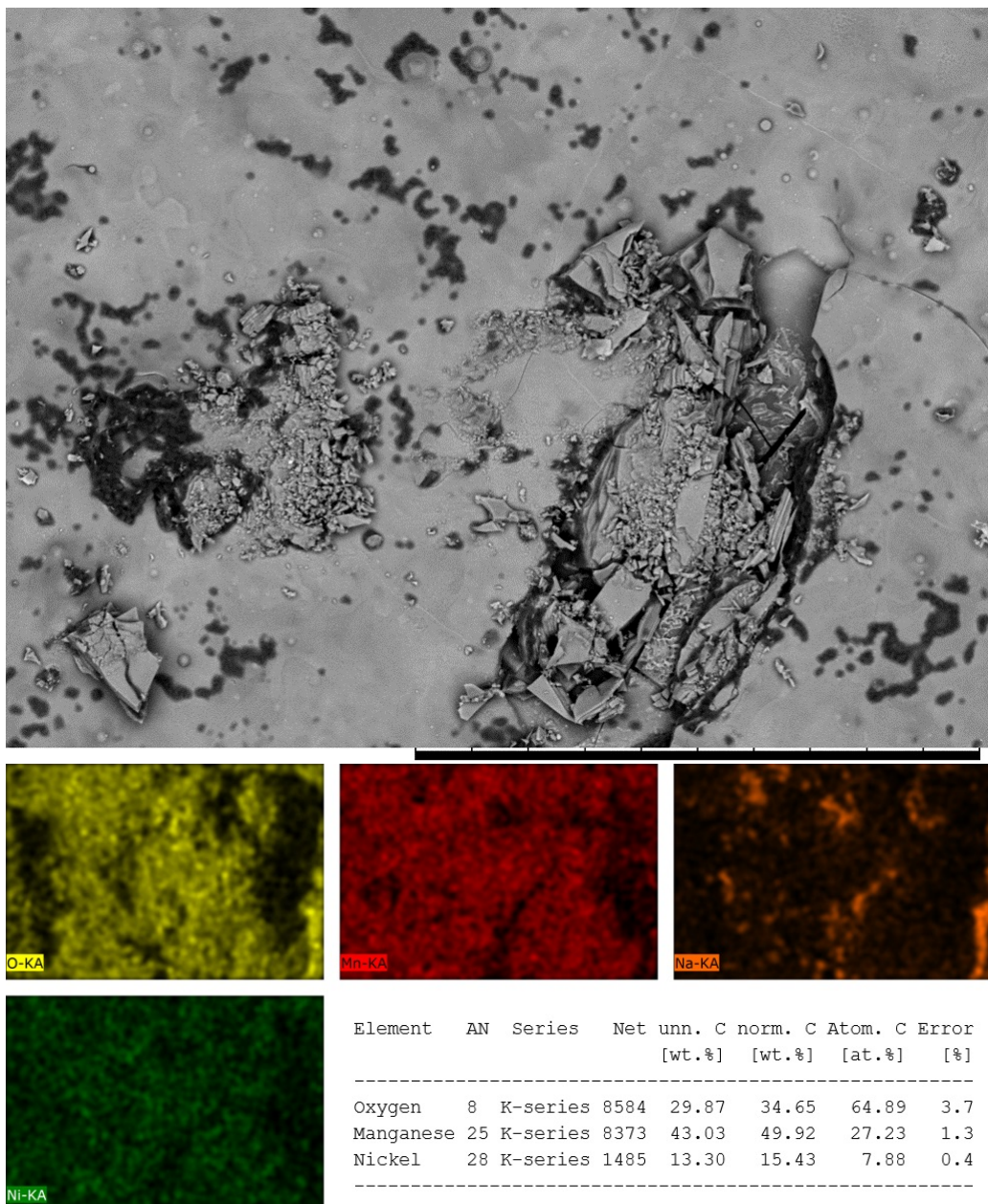


Figure 4.7: Agglomerates seen in 2.50 M LNMO probably resulting from an ensemble of particles interacting and agglomerating on the surface or on the tip of the injector-tube. The agglomerate seems to be mainly composed of LNMO.

4.2.2 XRD

The structures of the synthesised oxides were explored by XRD, and the obtained diffractograms are presented in the following section.

MnO₂

As quite evident in the diffractogram presented in figure 4.8, the oxide synthesised by injecting Mn(NO₃)₂ · 5 H₂O into the system at a temperature of 350–400°C and a pressure between 5 and 8 mbar is Mn₂O₃ and not the desired MnO₂. It could be tempting to say that there is some evidence of the (110) reflection of MnO₂ at 28.703 °coresponding to the tetragonal phase of MnO₂ with space group *P4₂/mnm*. However, the signal to noise ratio is too high to take this as a valid argument. Instead, the diffractogram turns out to be a good fit for Mn₂O₃ bixbyite with space group Ia-3. For simplicity, the Mn₂O₃ will mostly be referred to as MnO₂ throughout the thesis since this was the believed structure when performing the electrochemical analyses. Comparison of the diffractograms from the oxide at different concentrations show the 0.25 M to be a better fit than 2.50 M, since the latter contains more noise and lacks several of the peaks present at the low-concentration oxide.

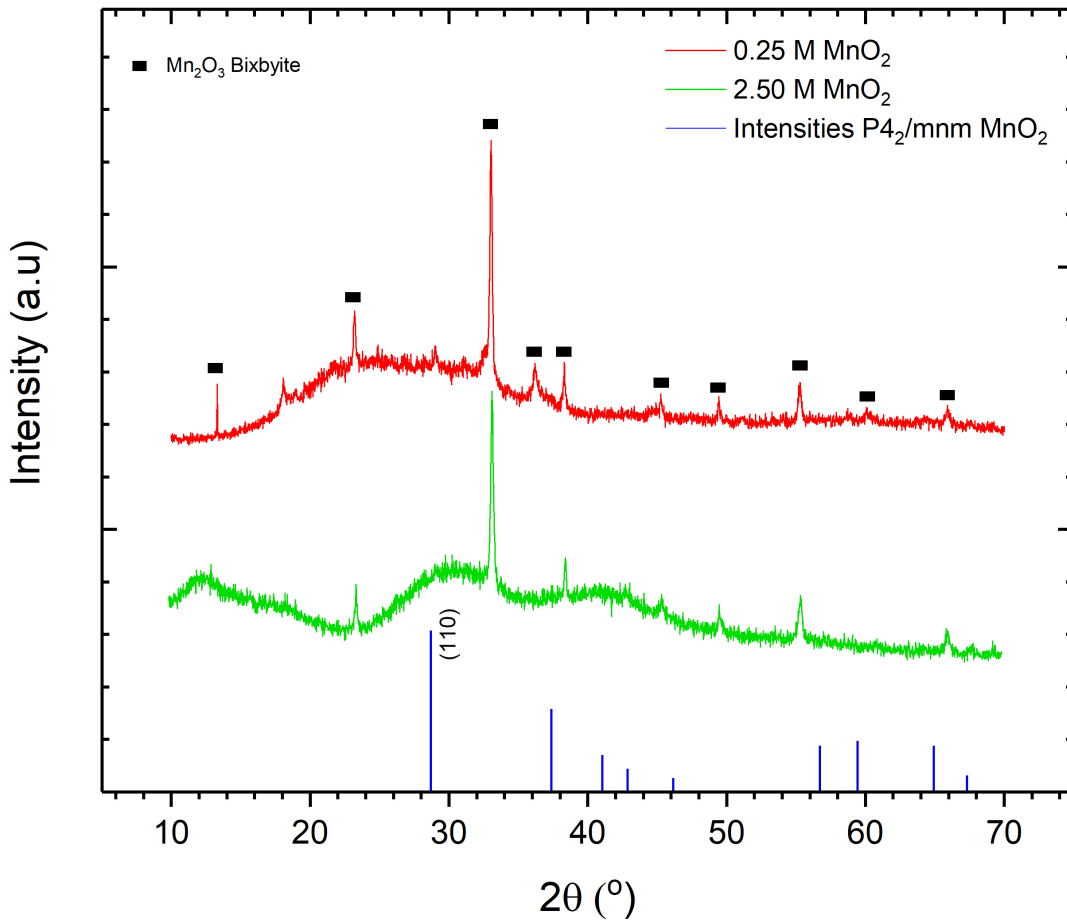


Figure 4.8: XRD of the oxide thought to be MnO₂. Analysis shows this to be quite a good match for Mn₂O₃ Bixbyite.

LMO

The diffractogram of LMO seen in figure 4.9 confirms that cubic LMO with space group Fd-3m is present. However, for 0.25 M LMO (red), there is also evidence of Mn_2O_3 bixbyite and some unidentified phase. Several attempts were made to identify this John Doe phase using the EVA software. When no derivative of manganese presented themselves as a solution, various compounds containing Ni, C and Si in addition to the expected Li, Mn and O were tested, thinking the signal could result from non-decomposed nitrates, impurities stemming from carbon or the Si present in the Si gel used to tighten the connectors. Unfortunately, none prevailed. Interestingly, the peaks of bixbyite disappears from 0.25 M LMO to 2.50 M LMO (green). At the same time, the peaks from LMO also seems to diminish, leaving two unidentified peaks.

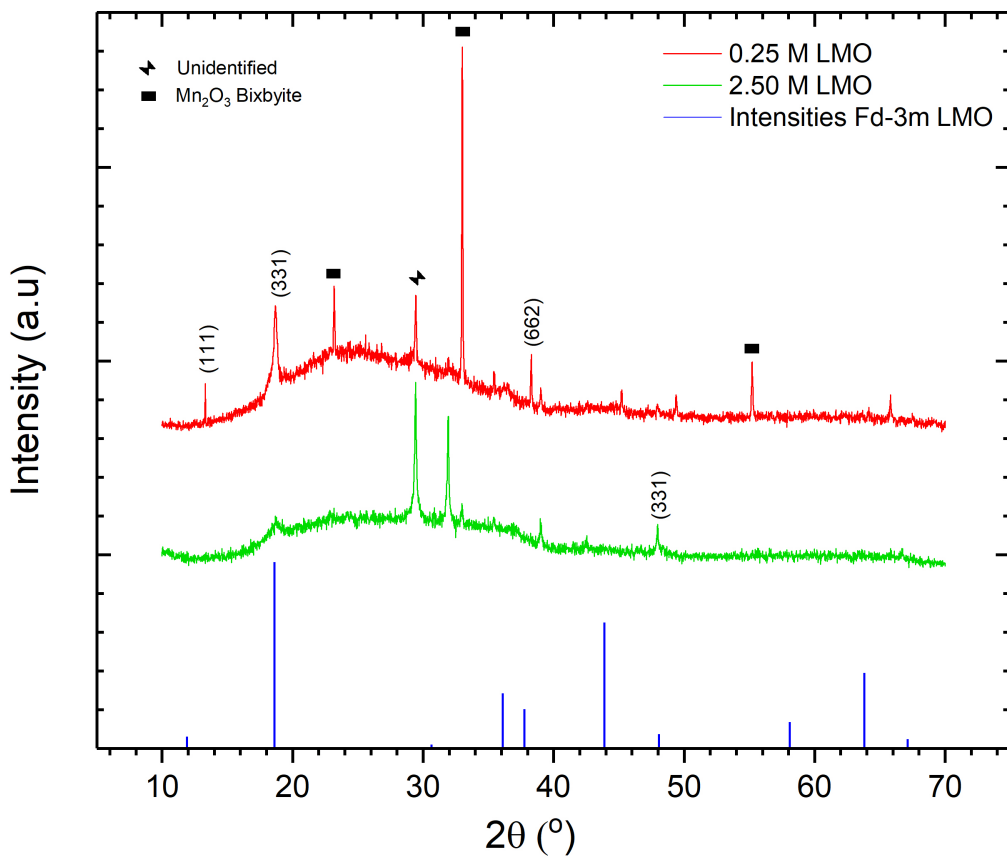


Figure 4.9: XRD of LMO. Analysis confirms that LMO is present, together with bixbyite for 0.25 M LMO and an unidentified phase for both the samples.

LNMO

Finally, the diffractogram for LNMO, presented in figure 4.10 exhibits a good correlation with literature intensities of cubic LNMO (Fd-3m). As expected, both LNMO samples show strong spinel structure peaks at $2\theta = 18.75^{\circ}, 36.40^{\circ}, 44.32^{\circ}$ and 64.44° and shows good correspondence to the XRD spherical LNMO presented in [16]. Interestingly, the same unidentified peaks found in LMO are also present here, to a great extent in 0.25 M

(red) and less in 2.50 M (green) LNMO. Also worth noting are the broad peaks corresponding to LNMO. Broad peaks are an indication of very small particles, which backs up the presence of crystallites seen in the SEM.

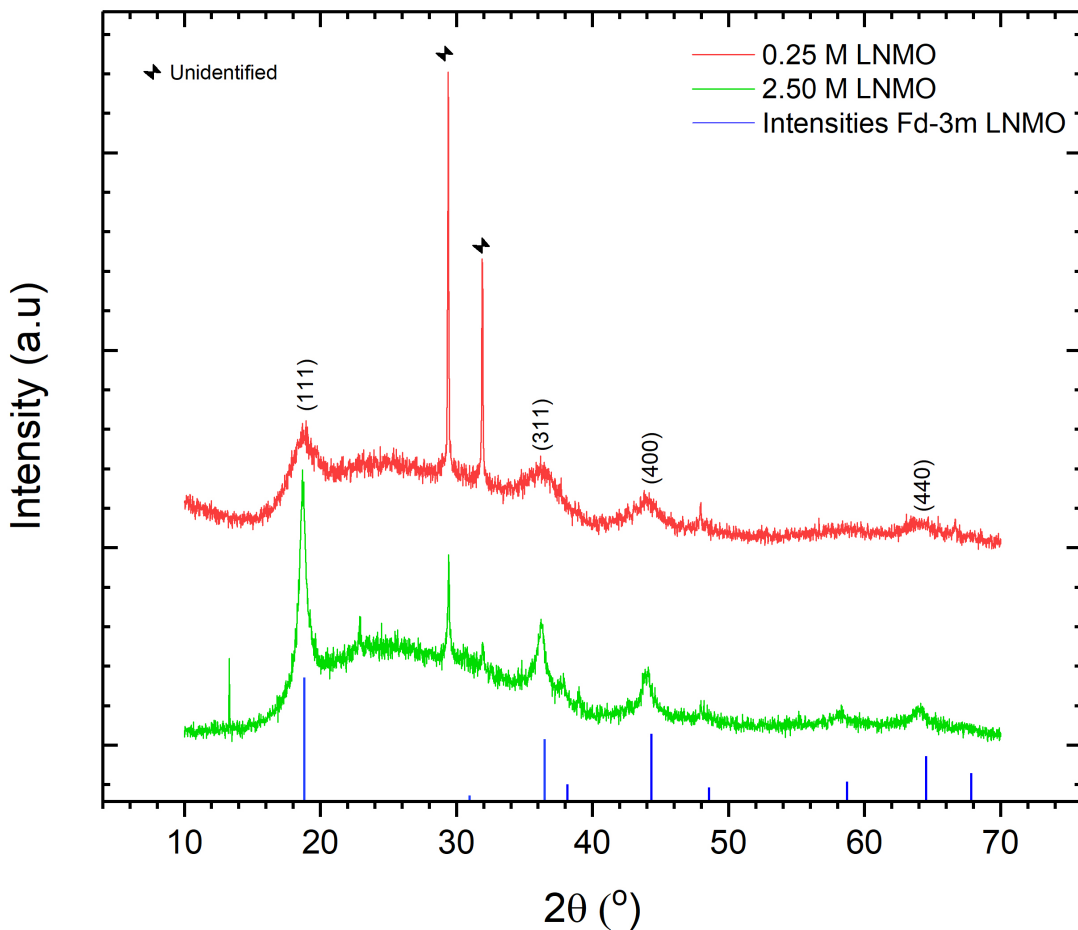


Figure 4.10: XRD of LNMO. The broad peaks correlate with literature intensities of LNMO and correspond to a small particle size, supporting the findings from the SEM. The same unidentified peaks are present in LMO and here.

4.3 Electrochemical analysis

The following section will deal with the electrochemical aspects of the coin cells assembled with the as-deposited oxides as the cathode, explained in section 3.6. Both cathodes made from 0.25 M and 2.5 M of precursors were tested and are presented herein.

4.3.1 Electric Impedance Spectroscopy

Figure 4.11 shows a snippet of the Nyquist plot used to present the EIS measurements performed on all the different cells and compares them with two commercial LMO cells, termed 'Ref LMO'. The linear contribution extrapolated to the x-axis gives an indication of the internal resistance in each battery, not accounting for electrode polarization. Common for all the synthesised cells is a lower extrapolated value than the commercial cells,

indicating a generally lower internal resistance in cells with cathodes produced by liquid injection compared to commercial. This is a clear improvement probably resulting from the lack of a binder. Carbon is often added to the polymeric binders commonly used in order to increase its conductivity. Nonetheless, the absence of a binder is preferred over a carbonaceous binder.

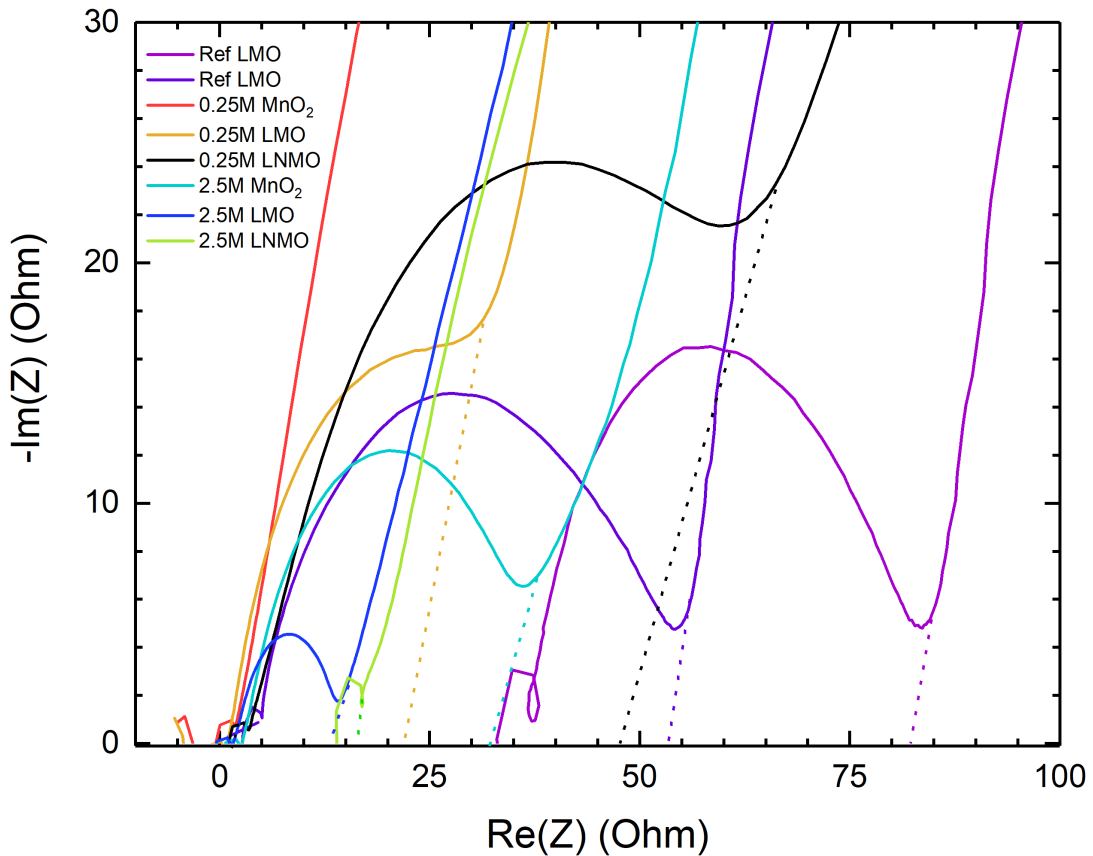


Figure 4.11: A Nyquist plot showing extrapolated EIS results compared to two commercial LMO battery cells. The cells using cathodes synthesised by liquid injection show a lower internal resistance than the commercial cells. The reference plots are reproduced with kind permission from Katja S.S. Sverdlilje.

4.3.2 Cyclic Voltammetry

CV is quite versatile, supplying both information regarding the occurrence of chemical reactions during charge-discharge and the capacity of the battery. Figure 4.12 displays the second cycle for the different cells. Cycle 2 is chosen due to the formation of SEI during the first cycle.

Figure 4.12 (a) and (b) shows the two different concentrations of the oxides thought to be MnO_2 , but in reality is Mn_2O_3 . The two curves present in (a) come from two different cathodes synthesised in the same process of liquid injection. For all the curves, there is a peak at 4 V. Looking closely at the green curve, there might in fact be two peaks that

are smeared and thus look like one. In the literature, this peak is often credited to the redox reaction of Mn^{4+}/Mn^{3+} which might indicate that there are in fact traces of MnO_2 in the cathode [16].

The apparent peak at 4.5 V arises since this is the point where the scanned potential is turned around. The peak is an indication of capacitance - charge is accumulated on the surface causing the current to increase with the applied potential until the scan direction is reversed.

Further in (a), the curves are mostly composed of a positive current. This could originate from several factors. Since the mass of the active material of the cathode is very small, there might be a leakage current which turns out to be significant when compared to the charge-discharge currents. Another possible explanation for the positive current is some reaction between Mn and the electrolyte taking place at the electrode-electrolyte interface. Of the two, the leakage current seems more plausible.

Moreover, due to the large uncertainty in recorded masses for these cathodes, the currents displayed on the y-axis of (a) and (c) are not to be trusted. There is not much evidence of chemical reactions occurring at all on discharge for either of the curves in (a) and (b) except a tiny bump at 4.1 V indicating capacitive behaviour.

In figure 4.12 (c) and (d), the different concentrations of LMO are presented. In (c), the whole curve is above 0 mA/g. Again, this may be due to erroneous mass, leakage current and/or chemical reactions on electrode-electrolyte interface. Either way, the curve shows a broad peak around 4 V. Similar to (a) and (b), the peak may in fact be composed of two peaks, as seems likely on discharge. In that case, the peaks correspond to the deintercalation/intercalation of Li^+ [35]. There is also evidence of capacitive characteristics for all the curves in both (c) and (d), especially in the green curve of (d) corresponding to cathode 31. Due to this, the cathode was cycled at different scan speeds as further discussed later in this section.

Similar to (c), the blue curve in (d) shows peaks at 4 and 4.15 V upon both charge and discharge, again corresponding to the two-step spinel reaction [16].

Lastly, figure 4.12 (e) and (f) displays cycle 2 from the results of cycling LNMO at the different concentrations. In (e), both curves display a peak around 4.15 V, but there is a huge height difference. There are also similar peaks at 4.7 V. This peak is present in the curve for cathode 52 (green) in (f) as well, but rather absent with cathode 51 (red). Instead, this curve shows a peak at 5 V on charge and 4.5 V on discharge. An increased peak-to-peak separation is evidence of higher resistance in the battery [28]. At the same time, the increased area under the curve indicates a higher capacity.

The peak at 4.7 V corresponds to Ni^{2+}/Ni^{4+} while the peak around 4.0 V, similar to LMO and MnO_2 , originates from the side reaction of Mn^{4+}/Mn^{3+} . As described in [16], homogeneous metal ion ordering results in a larger 4.7 V peak, while a more non-uniform distribution of Ni and Mn leads to a larger peak at 4V. Thus, cathode 24 appears to have a highly non-uniform distribution of Mn and Ni.

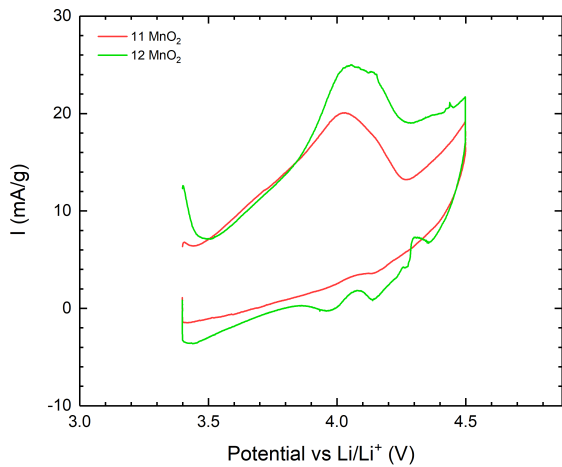
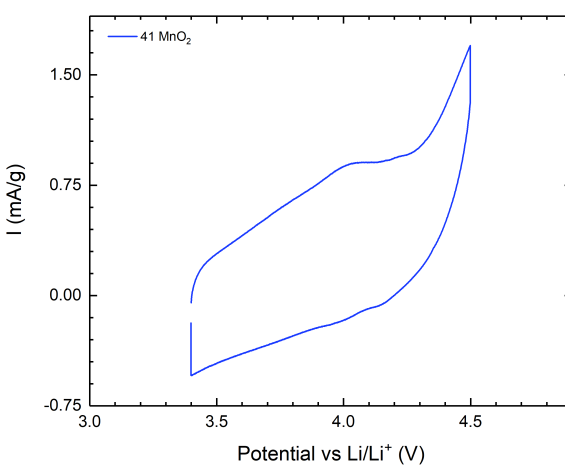
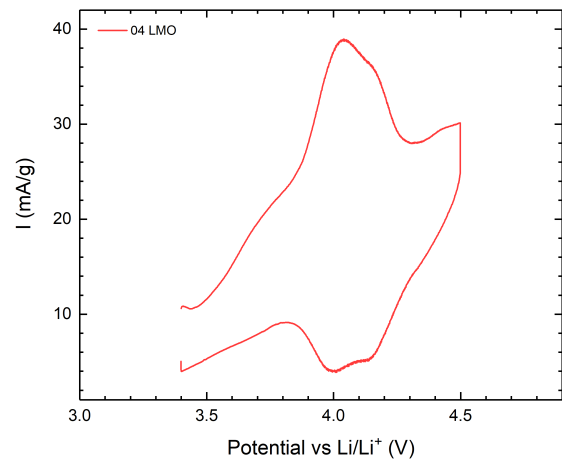
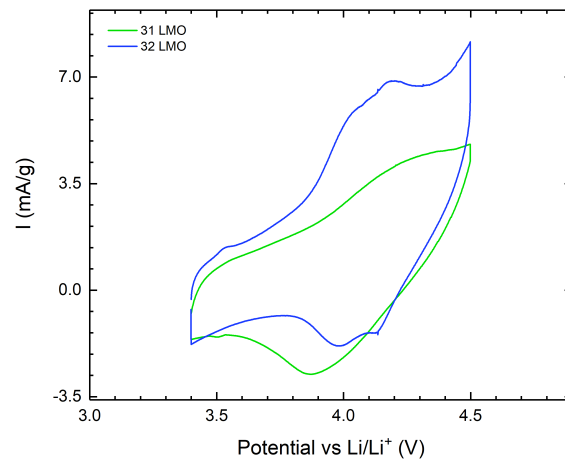
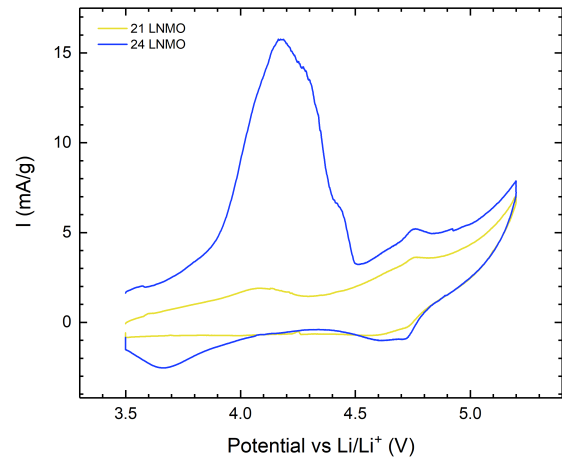
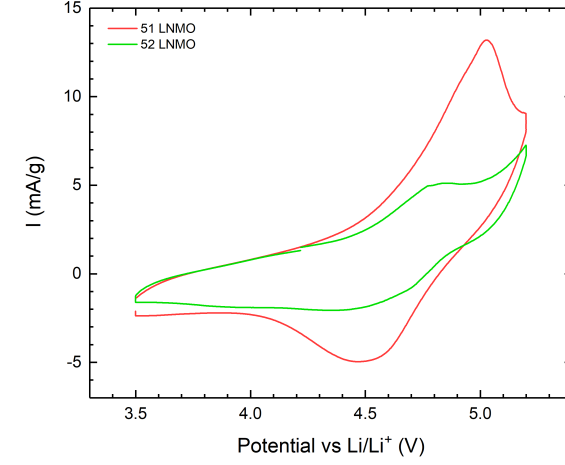
(a) MnO_2 at low concentration.(b) MnO_2 at high concentration.(c) LMO at low concentration.(d) LMO at high concentration.(e) $LNMO$ at low concentration.(f) $LNMO$ at high concentration.

Figure 4.12: Cycle 2 of CV performed for the different concentrations and electrode materials. The figure contains cycles of all the different synthesised oxides at high and low concentration of cations in the precursor solution.

In order to further investigate the behaviour seen in figure 4.12 (e), figure 4.13 displays all the cycles obtained from the CV of the cells containing cathodes 21 and 24. By looking at the first cycles for both (a) and (b), it is evident that the peak at 4 V is diminishing through the cycles until it disappears somewhere around the 5th cycle in (a) and 9th cycle in (b). It appears as though there is LMO present on the cathodes which transitions to LNMO during cycling, leaving only the peak at 4.7. The observed behaviour may also be due to the formation of an SEI. Often, the SEI is formed during the first one or two cycles. Sometimes, however, the SEI is formed over more cycles, which could be the case here.

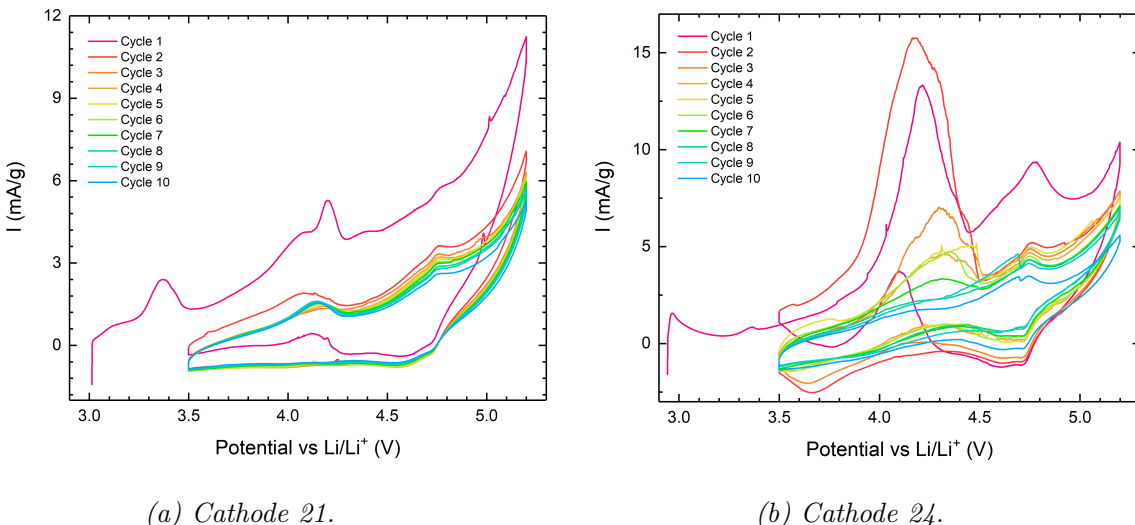


Figure 4.13: Full CV of LNMO corresponding to the cycles seen in figure 4.12 (e). Peaks that correspond to LMO or SEI formation are present for the first cycles, but diminishes after about 5 cycles (a) and 9 cycles (b).

Capacitor

The scan rate of the CV controls how fast the applied potential is scanned. The cell seen in figure 4.12 (d) was tested at different scan rates (mV/s) to see which effect this had. As can be seen in figure 4.14, this cell is behaving more and more as a capacitor with the increased cycling speed. The capacitor-like behaviour is evident from the shape shifting from the classical duck-shape to a rectangular shape, indicating the accumulation of charge on the surface of the cell on charge and dispersion of this charge upon discharge. There is no evidence of any chemical reaction taking place, and thus this is not a functional battery.

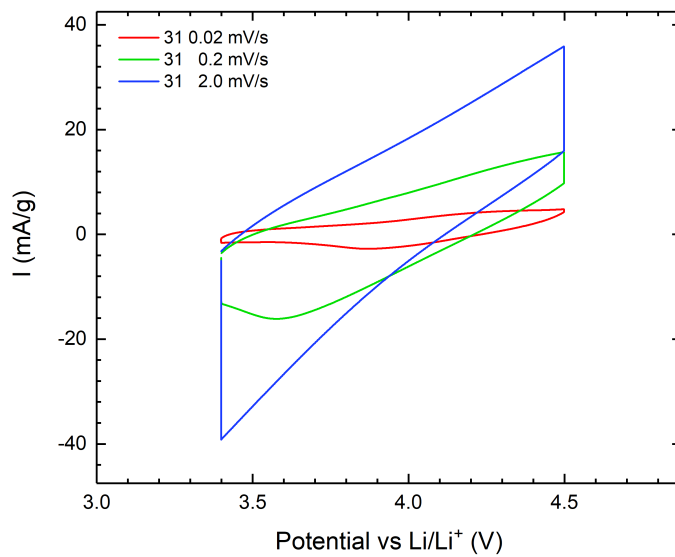


Figure 4.14: High concentration LMO run at different cycling speeds. This cell is clearly operating as a capacitor, especially at high scan rates.

4.3.3 Galvanostatic Cycling

Figures 4.15 and 4.16 show the results from galvanostatic cycling of the high-concentration cathodes for MnO₂ and LMO, respectively. Ideally, the same capacity obtained on charge should be obtained on discharge. The lines crossing the y-axis on 4.5 V shows the specific capacity on charge, while the lines crossing at the lower x-axis supplies the specific capacity on discharge. For MnO₂, the specific capacity is not notably high. However, the plot suggests that most of the energy entering the battery on charging is also leaving the battery on discharge. Still, there are no apparent plateaus corresponding to chemical reactions occurring, thus suggesting this cell to be a capacitor. The same is not true for LMO. Here, about 60-70 % capacity is lost during discharge, but there are traces of plateaus around 4.15 V corresponding to one of the peaks evident in the CV. Thus, this cell seems to be a functional battery cell, albeit not a very good one.

An attempt was made to measure GC of a LNMO cathode as well. However, probably due to surface polarisation, these measurements did not provide any readable data.

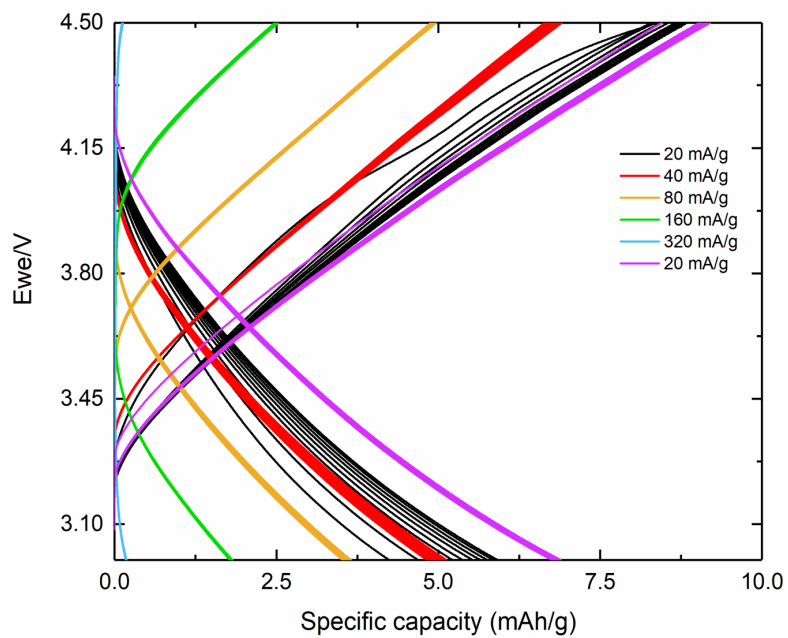


Figure 4.15: GC of $MnO_2(Mn_2O_3)$. Due to a lack of plateaus, this cathode appears to be purely capacitive.

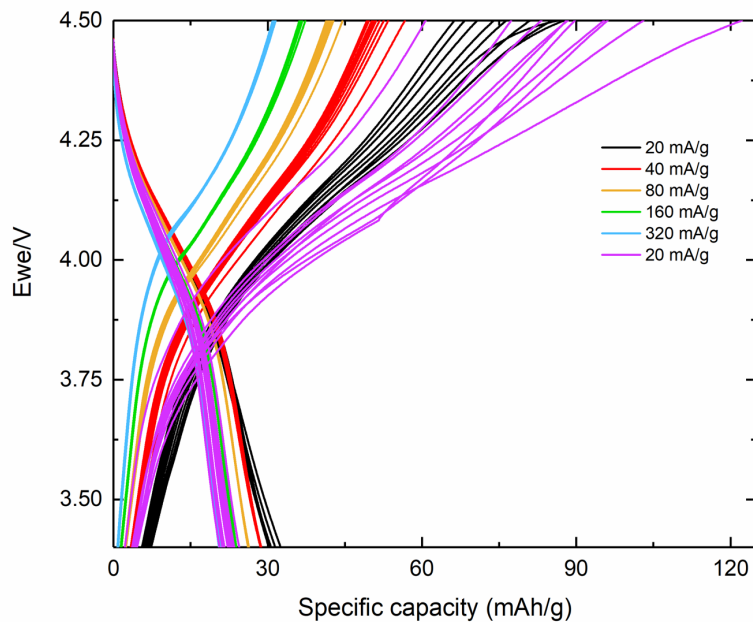


Figure 4.16: GC of LMO. This plot shows plateaus at 4.15 V corresponding to one of the observed peaks in the CV plots. This cathode appears to be electrochemical, albeit with a poor discharge capacity.

5

Conclusion

The liquid injection system presented here is far from perfect for the synthesis of cathode materials due to a lack of precision regarding the synthesised oxides and several of said oxides yielding cathodes with capacitive behaviour. Nevertheless, the system has proved capable of synthesising some of the desired oxides which adhered to a steel substrate and was thus able to be used as the cathode in a cell without further modification. The morphology seemed to mainly consist of hollow, porous spheres which has been reported as advantageous in cathodes due to factors such as rapid diffusion and enhanced rate capability.

Indeed, the electrochemical analyses showed that chemical reactions were occurring in most of the cells, indicating that the cells can be used in batteries, preferably after some further modifications. The low resistance shown by the EIS is very promising for the notion of synthesizing cathode materials without the need for a binder.

In general, the synthesised cathodes exhibit lower internal resistance than commercial LMO cathodes, but it is difficult to read the electrochemical reactions.

Further improvements and research could be done by achieving greater control of the deposition parameters, ideally obtaining similar deposited masses for consecutive syntheses. Furthermore, it would be interesting to see cathodes with even more active material, possibly achieved by injecting a greater volume during liquid injection. Lastly, another attempt should be made at synthesising MnO_2 by lowering the temperature.

In conclusion, this work has expanded the understanding of the liquid injection system in vacuum and the effect of different parameters, and proved this process to be a candidate for the synthesis of low-resistance cathode materials.

Bibliography

- [1] K. B. Gandrud, “Thin film materials for li-ion batteries made by atomic layer deposition,” PhD thesis, UiO, 2014, pp. 3–10, 37–44.
- [2] K. Zaghib, A. Mauger, and C. Julien, “Overview of olivines in lithium batteries for green transportation and energy storage,” *Journal of Solid State Electrochemistry*, vol. 16, no. 3, pp. 835–845, 2012.
- [3] N. Nitta, F. Wu, J. T. Lee, and G. Yushin, “Li-ion battery materials: Present and future,” *Materials Today*, vol. 18, no. 5, pp. 252–264, 2015.
- [4] B. Dibner, *Alessandro Volta and the electric battery*, eng, ser. Immortals of science. New York: Franklin Watts, 1964.
- [5] R. Yazami and P. Touzain, “A reversible graphite-lithium negative electrode for electrochemical generators,” *Journal of Power Sources*, vol. 9, no. 3, pp. 365–371, 1983.
- [6] R. Moshtev and B. Johnson, “State of the art of commercial li ion batteries,” *Journal of Power Sources*, vol. 91, no. 2, pp. 86–91, 2000.
- [7] J. B. Goodenough and K.-S. Park, “The li-ion rechargeable battery: A perspective,” *Journal of the American Chemical Society.*, vol. 135, no. 4, pp. 1167–1176, 2013.
- [8] A. Yoshino, “The birth of the lithium-ion battery,” eng, *Angewandte Chemie International Edition*, vol. 51, no. 24, pp. 5798–5800, 2012.
- [9] H. Vikström, S. Davidsson, and M. Höök, “Lithium availability and future production outlooks,” *Applied Energy*, vol. 110, pp. 252–266, 2013.
- [10] P. Gruber, P. Medina, G. Keoleian, S. Kesler, M. Everson, and T. Wallington, “Global lithium availability a constraint for electric vehicles?” English, *Journal Of Industrial Ecology*, vol. 15, no. 5, pp. 760–775, 2011.
- [11] J. Speirs, M. Contestabile, Y. Houari, and R. Gross, “The future of lithium availability for electric vehicle batteries,” English, *Renewable & Sustainable Energy Reviews*, vol. 35, no. C, pp. 183–193, 2014.
- [12] H. Sanderson and C. Cornish, “Amnesty warns on use of child labour in cobalt mining,” *Financial Times*, Nov. 2017. [Online]. Available: <https://www.ft.com/content/bec64762-c923-11e7-ab18-7a9fb7d6163e>, [Accessed on 1 June 2018].
- [13] M. Augustin, D. Fenske, I. Bardenhagen, A. Westphal, M. Knipper, T. Plaggenborg, J. Kolny-Olesiak, and J. Parisi, “Manganese oxide phases and morphologies: A study on calcination temperature and atmospheric dependence,” English, *Beilstein Journal Of Nanotechnology*, vol. 6, no. 1, pp. 47–59, 2015.
- [14] Ş. Özcan, A. Güler, T. Cetinkaya, M. O. Guler, and H. Akbulut, “Freestanding graphene/MnO₂ cathodes for li-ion batteries,” eng, vol. 8, no. 1, pp. 1932–1938, 2017.

- [15] Yirong, Zhou, Tong, Chen, Junxi, Zhang, Yao, Liu, Ping, and Ren, “Amorphous MnO₂ as cathode material for sodium-ion batteries,” vol. 35, no. 08, pp. 1294–1298, 2017.
- [16] J. Wang, W. Lin, B. Wu, and J. Zhao, “Porous LiNi_{0.5}Mn_{1.5}O₄ sphere as 5 v cathode material for lithium ion batteries,” *Journal of Materials Chemistry A*, vol. 2, no. 39, pp. 16 434–16 442, 2014.
- [17] J. K. Hong, J. H. Lee, and S. M. Oh, “Effect of carbon additive on electrochemical performance of LiCoO₂ composite cathodes,” *Journal of Power Sources*, vol. 111, no. 1, pp. 90–96, 2002.
- [18] D. S. Jung, Y. N. Ko, Y. C. Kang, and S. B. Park, “Recent progress in electrode materials produced by spray pyrolysis for next-generation lithium ion batteries,” *Advanced Powder Technology*, vol. 25, no. 1, pp. 18–31, 2014.
- [19] A. Kopp Alves, C. P. Bergmann, and F. A. Berutti, “Spray pyrolysis,” in *Novel Synthesis and Characterization of Nanostructured Materials*. Berlin, Heidelberg: Springer Berlin Heidelberg, 2013, pp. 23–30.
- [20] D. S. Jung, S. B. Park, and Y. C. Kang, “Design of particles by spray pyrolysis and recent progress in its application,” *Korean Journal of Chemical Engineering*, vol. 27, no. 6, pp. 1621–1645, 2010.
- [21] D. Perednis and L. J. Gauckler, “Thin film deposition using spray pyrolysis,” *Journal of Electroceramics*, vol. 14, no. 2, pp. 103–111, Mar. 2005.
- [22] J. B. Goodenough and K.-S. Park, “The li-ion rechargeable battery: A perspective,” eng, *Journal of the American Chemical Society*, vol. 135, no. 4, Jan. 2013.
- [23] M. Pinson and M. Bazant, “Theory of sei formation in rechargeable batteries: Capacity fade, accelerated aging and lifetime prediction,” English, *Journal Of The Electrochemical Society*, vol. 160, no. 2, A243–A250, 2013.
- [24] J. I. Goldstein, *Scanning Electron Microscopy and X-Ray Microanalysis*, eng, 2nd ed. 1992. 2018, ISBN: 1-4939-6676-6.
- [25] Y. Leng, “Scanning electron microscopy,” eng, in *Materials Characterization*, Wiley-VCH Verlag GmbH & Co. KGaA, 2013, pp. 127–161, ISBN: 9783527334636.
- [26] J. Als-Nielsen and D. McMorrow, *Elements of modern X-ray physics*, eng, 2nd ed. Chichester, West Sussex: John Wiley, 2011.
- [27] J. Scotman, “Synchrotron based operando methods for characterization of non-aqueous rechargeable battery electrode materials,” PhD thesis, UiO, 2017.
- [28] N. Elgrishi, K. J. Rountree, B. D. McCarthy, E. S. Rountree, T. T. Eisenhart, and J. L. Dempsey, “A practical beginner’s guide to cyclic voltammetry,” eng, *Journal of Chemical Education*, vol. 95, no. 2, pp. 194–206, Feb. 2018.
- [29] “Voltammetric techniques,” in *Inorganic Electrochemistry*, Cambridge: Royal Society of Chemistry, 2003, pp. 49–136, ISBN: 978-0-85404-661-4.
- [30] K. B. Kvamme, “Phosphites in atomic layer deposition: Synthesis and characterisation using unconventional phosphorous precursors,” UiO, 2016, pp. 2–28.
- [31] H.-H. Chang, C.-C. Chang, H.-C. Wu, M.-H. Yang, H.-S. Sheu, and N.-L. Wu, “Study on dynamics of structural transformation during charge/discharge of lifepo₄ cathode,” *Electrochemistry Communications*, vol. 10, no. 2, pp. 335–339, 2008.

- [32] P. K. Gallagher, F. Schrey, and B. Prescott, “The thermal decomposition of aqueous manganese (ii) nitrate solution,” *Thermochimica Acta*, vol. 2, no. 5, pp. 405–412, 1971.
- [33] M. L. Ruiz, I. D. Lick, M. I. Ponzi, E. R. Castellón, A. Jiménez-López, and E. N. Ponzi, “Thermal decomposition of supported lithium nitrate catalysts,” *Thermochimica Acta*, vol. 499, no. 1, pp. 21–26, 2010.
- [34] W. Brockner, C. Ehrhardt, and M. Gjikaj, “Thermal decomposition of nickel nitrate hexahydrate, $\text{Ni}(\text{NO}_3)_2 \cdot 6 \text{H}_2\text{O}$, in comparison to $\text{Co}(\text{NO}_3)_2 \cdot 6 \text{H}_2\text{O}$ and $\text{Ca}(\text{NO}_3)_2 \cdot 4 \text{H}_2\text{O}$,” *Thermochimica Acta*, vol. 456, no. 1, pp. 64–68, 2007.
- [35] Y. Wang, Y. Wang, D. Jia, Z. Peng, Y. Xia, and G. Zheng, “All-nanowire based li-ion full cells using homologous Mn_2O_3 and LiMn_2O_4 ,” *Nano Letters*, vol. 14, no. 2, pp. 1080–1084, 2014.